STRUCTURAL PROPERTIES AND OPTICAL MODELLING OF SiC THIN FILMS

FATEMA ABDALLAH MUSA AHMED

A thesis submitted in partial fulfilment of the requirements for the degree of Magister Scientiae in the Department of Physics and Astronomy, University of the Western Cape.

Supervisor: Dr. S. Halindintwali (UWC)

Co-supervisor: Prof. C.J. Arendse (UWC) & Dr. O. Nemraoui (CPUT)

January 2020

KEYWORDS

Thin films

Amorphous silicon carbide

Electron-beam

Annealing

Stoichiometry

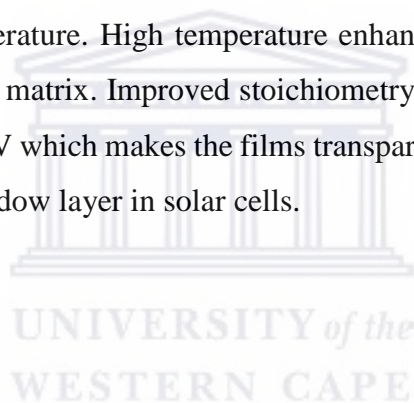Structural properties

Si-C concentration

Optical modelling

Effective medium approximation theory

Band gap

ABSTRACT

Amorphous silicon carbide (a-SiC) is a versatile material due to its interesting mechanical, chemical and optical properties that make it a candidate for application in solar cell technology. As a-SiC stoichiometry can be tuned over a large range, consequently is its bandgap. In this thesis, amorphous silicon carbide thin films for solar cells application have been deposited by means of the electron-beam physical vapour deposition (e-beam PVD) technique and have been isochronally annealed at varying temperatures. The structural and optical properties of the films have been investigated by Fourier transform Infrared and Raman spectroscopies, X-ray diffraction, Scanning Electron Microscopy, Energy Dispersive X-ray Spectroscopy and UV-VIS-NIR spectroscopy. The effect of annealing is a gradual crystallization of the amorphous network of as-deposited silicon carbide films and consequently the microstructural and optical properties are altered. We showed that the microstructural changes of the as-deposited films depend on the annealing temperature. High temperature enhances the growth of Si and SiC nanocrystals in amorphous SiC matrix. Improved stoichiometry of SiC comes with high band gap of the material up to 2.53 eV which makes the films transparent to the visible radiation and thus they can be applied as window layer in solar cells.

January 2020

iii

DECLARATION

I declare that *Structural Properties and Optical Modelling of SiC Thin Films* is my own work, that it has not been submitted for any degree or examination in any other university, and that all the sources I have used or quoted have been indicated and acknowledged by complete references.

Fatema Abdallah Musa Ahmed   January 2020

Signed:

DEDICATION

To myself Fatema

ACKNOWLEDGEMENTS

I am very grateful for Allah for giving me the strength to carry out this work.

I would like to thank and express my appreciation for the following people:

My supervisor Dr. S. Halindintwali, who have supported and always been ready to guide me throughout this thesis. I would like also to express my sincere gratitude to my co-supervisors Dr. O. Nemraoui at (CPUT) and Prof. C. Arendse at (UWC), for their encouragement and support.

Dr. C. Mtshali, of the Material Research Department iThemba LABS, for his assistance with electron-beam deposition samples.

Mr. T. Lesch, at the Department of Chemistry (UWC), for his assistance with the FTIR measurements.

Dr. R. Butcher, of the Material Research Department iThemba LABS, for his assistance with the XRD measurements.

Mr. E. Mc Donald, of the Electron Microscope Unit at UWC, for his assistance with the SEM/EDX measurements.

Dr. S. Khamlich, of the Material Research Department iThemba LABS, for his assistance with UV-VIS-NIR measurements.

The Organization for Women in Science for the Developing World (OWSD) and Swedish International Development Cooperation Agency (Sida), for their financial assistance.

Many thanks to all family, especially my mother for her love, prayers and duaa.

Finally, thanks to all my friends for our interesting discussions, support and their friendship throughout this journey.

Contents

CHAPTER 1

Introduction

1.1 Overview on Solar Energy

Energy consumption is increasing due to the growth in population and technological advancement. The role played by the fossil fuels such as coal, oil and natural gas in meeting the global energy demands cannot be overemphasized. However, the release of carbon oxides in the atmosphere as a result of utilization of fossil fuels is an unacceptable consequence. Carbon oxides and other greenhouse gases adversely influence the balance of the earth's temperature. The devastation caused by the altered atmospheric composition can constitute a monumental impact on weather and climatic conditions such as increased global temperature, sea levels and unpredictable weather patterns [1]. Provision of alternative sources of energy can mitigate the production of greenhouse gases and consequently reduces the global warming. Renewable energy technologies are being considered as potential alternative sources for future global energy supply.

Solar energy is considered as the main renewable energy source, which can meet the high energy demand worldwide. It is an abundant, clean, sustainable, and reliable energy source. Solar energy can be usually converted to electrical or other forms of energy. The conversion can be exploited in different ways such as photovoltaic cell and solar thermal. Photovoltaics is the most favourable technology used to convert solar power into electricity. The Photovoltaic cell make use a semiconductor material to convert solar light from the sun to electrical energy. A sphere of gases consisting of hydrogen and helium are the primary constituents of the sun. These gases, when heated at very high temperature in the core of the sun, undergo nuclear fusion and one of the by-products is the emission of electromagnetic radiation. The emitted radiation has wavelengths that are similar to that of black body radiation at 5250 ^{0}C as shown in fig1.1. The solar radiation received on earth is 1.5×10^{18} kWh/year [2], which is ten thousand times higher than the global energy demands. Consequently, the potential in energy supply offered by solar radiation is huge.

https://etd.uwc.ac.za/
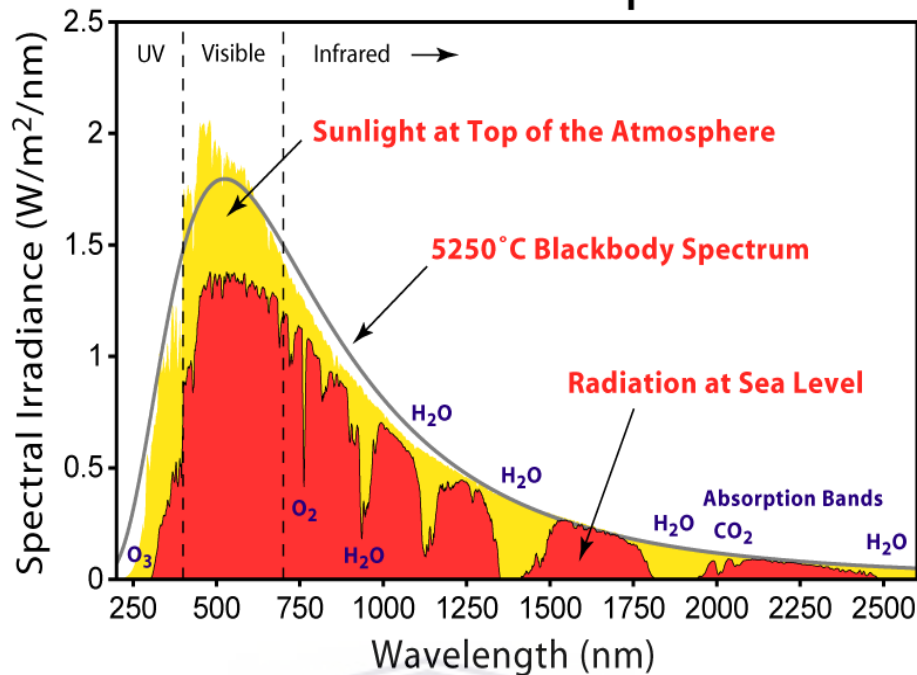
Figure 1.1: A blackbody emits different spectra according to the temperature of its surface [3].

1.2 Photovoltaic Technology

The first generation photovoltaic cells are primarily made up of silicon wafers. The advancement in photovoltaic technology has been hampered by high cost production of solar cells. The relative high cost of materials for the production of first generation of photovoltaic solar cell led to the production of second generation solar cells, which is the thin film photovoltaic solar cells. These materials come with significant reduction in production cost, because of required small thickness of the layers as well as the relaxation in requirements of high purity silicon wafer. The unit of manufacturing in the thin film of glass sheet ~ 1 m^2 for photovoltaic solar cells is therefore about 100 times higher than silicon wafers of ~ 100 cm^2 with possibility of higher energy conversion [4]. The thin film photovoltaic solar cells share the same performance restrictions for single-junction devices, which is known as Shockley–Queisser limit as the conventional Si devices [5]. The reduction in manufacturing cost in thin film photovoltaic solar cells is a consequence of a reduced manufacturing costs and the use of lower quantity of material.

2

Shockley and Queisser [5] suggested higher spectral conversion efficiency for the second generation solar cell, but this does not lead to the power conversion efficiency. The efficiency limits of thin film solar cells can be influenced by the thermal relaxation losses, due to photons of energy higher than the band gap and transmission losses, due to the photons carrying energies lower than the band gap. The photovoltaic cells with higher conversion efficiencies should be expected from the third generation of photovoltaic solar cells. The transmission losses in the second-generation solar cells are the main cause of reduced spectral conversion efficiency and this triggered the emergence of the third generation solar cells technology. It consists in the use of the multi-junction materials. The superimposed sub-cells in a multi-junction stacks with semiconductor materials of different bandgap values, allows the photon absorption in an extended range of the spectrum. Third generation photovoltaic cells provide thus a more efficient spectral conversion and it is a step forward in overcoming the Shockley-Queisser theoretical limit of single bandgap devices. Currently, a higher conversion efficiency based on multi-junction solar cells achieved up to 46.0% [6 , 7].

1.3 Semiconductor Silicon Carbide Material

Silicon carbide (SiC) has received much attention in electronic devices and microelectromechanical systems (MEMS), due to its superior properties such as a wide band gap, high melting temperature, high elastic modulus, high fracture toughness, high hardness, chemical inertness and good thermal conductivity [8 –11]. It can be used as a protective coating instead of silicon, due to its toughness and excellent mechanical properties that make it candidate for use in harsh environments [9,12]. The thermal and chemical stability of SiC is superior compared with the other high bandgap semiconductors such as GaN and ZnSe [13]. It is therefore, commonly used for high temperature and high power applications. It is high bandgap ensures high transparency in most of the visible part of the spectrum and as a result, SiC can be used as window layer [14,15]. SiC can be grown in amorphous and microcrystalline thin films. For instance, Chen *et al.* [16] reported that an improvement of conversion efficiency of the solar cell of $\eta = 9.6\%$ with a successful application of microcrystalline silicon carbide as window layer with an optical bandgap of $E_g^{opt} = 2.8$ eV.

Exploitation of the structural and optical properties of silicon carbide films requires a good understanding of the correlation between these properties and the technological applications in devices. Hydrogenated amorphous silicon carbide (a-SiC: H) has been employed as a window layer in solar cells, because the optical gap (E_g^{opt}) of a-SiC can be increased constantly by increasing the carbon content in the films [17]. The available information on SiC has led to its application in passivation layers, anti-reflection coating, and even replacement of transparent conductive oxide TCO in crystalline silicon solar cells [18]. Silicon carbide can possess different structures, each within its own optical properties. Moreover, its polytypes can be transformed from one form to another depending on the temperature. In particular, the cubic silicon carbide (3C-SiC) has been of great interest in solar cells technology.

A tetrahedral frame of all polytypes can be presented as a silicon atom in the centre surrounded by carbon atoms and vice versa. The distance between covalently bonded silicon and carbon atoms is about 1.89 A^o. Meanwhile, the lattice constant which is length of sp^3 bonding between Si-Si and C-C is approximately 3.08 A^o as shown in fig 1.2.
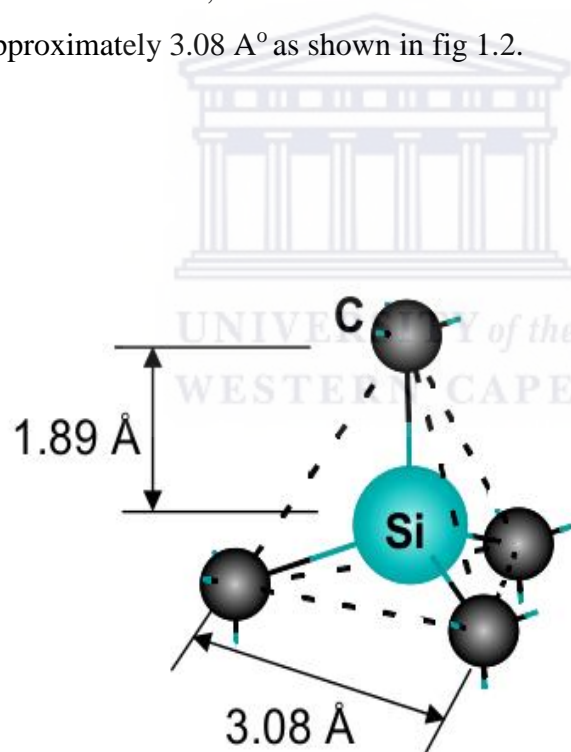
Figure 1.2: Tetrahedral structural of SiC [19].

1.4 Crystallographic Structure of Silicon Carbide

Silicon carbide is a stable compound of Si and C atoms that can exist in long-range ordered structures. It can be crystallized into a large variety of polytypes. The polytypism phenomenon occurs during the rotation of the stacking sequence of the double layer of Si-C atoms into three characteristic icons. The coordination types are identified as A, B, C. as in fig 1.3.
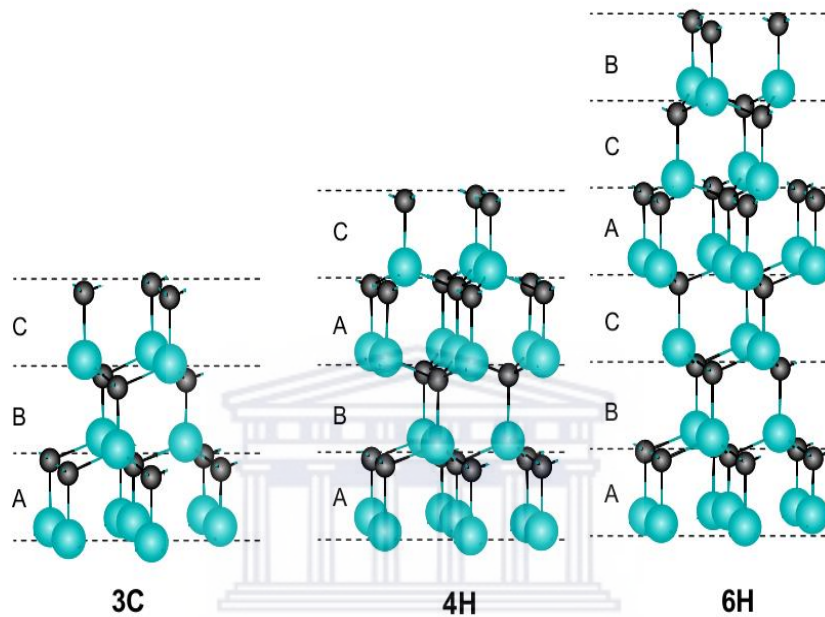
Figure 1.3: Schematic diagram of the stacking sequence for the most common polytypes SiC cubic (3C) and hexagonal (4H and 6H) [19].

The variation of these double layers along the vertical axis referred to as c-axis, identifies polytypes of different physical and optical properties. The most common of the over 250 polytypes of SiC discovered are cubic 3C, and hexagonal 6H and 4H [20–22].

1.5 Amorphous Silicon Carbide Films

Amorphous silicon carbide (a-SiC) is well known for its applications as emitter of high-speed bipolar transistor (TBT), solar cells, microwave power transistor, light-emitting diodes and sensor [23]. a-SiC is a valuable material for silicon heterostructure for application in thin Si films solar cells and it can be prepared using a variety of deposition techniques.

5

The atomic structure of a-SiC is similar to that of amorphous silicon (a-Si) as both have short-range atomic order with a tetrahedral atomic coordination. However, there are differences in the bond lengths and bond angles compared to the Si-Si form of crystalline structure counterpart. An increased disorder in a-SiC in comparison with a-Si is noted, as a result of the intrinsic physical disorder of the material due to the additional Si-C bond as shown in fig 1.4.
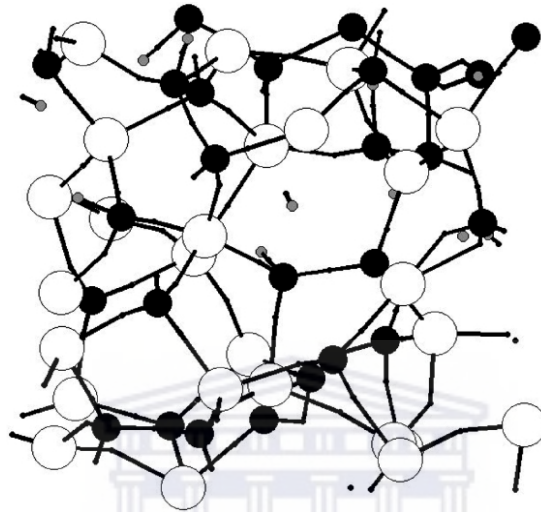
Figure 1.4: The disordered network of amorphous silicon carbide network, where white and black big balls represent silicon and carbon atoms, respectively. The structure also contains hydrogen atoms represented by small grey balls to form a-SiC:H [24, 25].

Amorphous silicon and silicon alloys are characterised by recombination centres also known as gangling bonds. Hydrogen atoms introduced into the a-SiC network play a vital role into compensating them. Thus in order to reduce the defect density, disorder structure and to prevent recombination of charge carriers in a-SiC films, hydrogen incorporation is desired [26]. Since, the bond C-H is stronger than Si-H bond, it is more stable against the Staeble-Wronski (SWE) degradation. The strength of the Si-C bond arises from the difference in electronegativity between Si and C atoms. Thus, the addition of hydrogen improves the quality of the a-SiC properties.

Amorphous silicon carbide has been investigated as a potential industrial material, which displays a range of structural, chemical, optical, electrical, and mechanical properties through

control of the variation of its individual elemental concentration. Since a-SiC can easily fabricated composition of varying stoichiometry, its properties can be tuned for application in a variety of fields. Moreover, the chemical and mechanical characteristics of a-SiC: H have been recognized as more outstanding than those of a-Si [27].

Furthermore, crystallization of amorphous SiC can be achieved through a convenient temperature annealing treatment, which leads to extreme changes into structural properties. Thus, an improvement in optical transparency and electrical conductivity of a-SiC$_x$ following progressive alteration of the network in gradual annealing process. In addition, the change in changing the bonding structure of a-SiC through variation in carbon content can also allow the control of the structure and optical properties of the material. Tianru *et al.* [28] found that the increase in the Si-C and C-H$_n$ results in the increase of the bandgap of a-SiC from 1.8 eV to 3.0 eV. Thus high C concentration leads to high bandgap materials, desirable for use as window layer for photovoltaic applications.

The chemical structure is influenced by the elemental concentration of Si and C and it can be arranged into two types of amorphous networks, namely silicon-rich amorphous silicon carbide (Si-rich a-SiC) or carbon-rich amorphous silicon carbide (C-rich a-SiC). Consequently, one can obtain Si nanocrystalline or C graphitic clusters under high temperature annealing of the amorphous SiC matrix. Si-rich amorphous SiC$_x$ films have been applied as transparent layers in solar cells, while C rich films have been used as an active layer in electroluminescent devices[29, 30].

The dielectric matrix of amorphous SiC is used to prepare silicon quantum dots to be used in photovoltaic applications as absorber layer in Si based tandem solar cells, because of the advantage of its optimized bandgap value of around 2.5 eV, lower than those of other Si related dielectric matrices such as SiO$_x$ and SiN$_x$, this reduced bandgap gives to SiC$_x$ a semiconductor character and thus better electrical transport properties [31].

The phase transition from amorphous into microcrystalline silicon carbide occurs when the material is exposed to high annealing temperatures or grown under high hydrogen dilution for instance. The preparation of good quality microcrystalline SiC at low temperature of the substrate is still under development and of intense research interest.

1.6 Aim and Outline of this Thesis

The objective of this thesis is to study the structural and optical properties of amorphous silicon carbide (a-SiC) of varied stoichiometry. In order to study the effect of silicon and carbon interaction alone, a-SiC$_x$ thin films have been prepared by electron beam physical vapour deposition technique. The films have been subjected to varied annealing temperatures in order to yield different microstructures. Different analytical techniques have been used to characterize the material.

Chapter 1: This chapter provides background literature on SiC material and addresses specific areas where they find application. It gives an overview highlights on the unique properties of SiC and presents the aim and outline of this thesis.

Chapter 2: This chapter gives an overview of the techniques commonly used for thin films deposition; in particular, the electron-beam physical vapour deposition used for most of the samples studied in the thesis, is discussed. It presents the experimental details used for films deposition.

Chapter 3: This chapter contains a concise review to analytical techniques utilized in this thesis, the analytical techniques includes FTIR, RS, XRD, SEM, EDX, and UV-VIS-NIR spectroscopy.

Chapter 4: This chapter is dedicated to the presentation and discussion of the experimental results. The emphasis is on structural and optical properties.

The last part of the thesis gives a summary of the results and it proposes recommendations for future work.

CHAPTER 2

Experimental Methods

This chapter gives an overview of the most commonly deposition techniques used to grow SiC materials. Moreover, this chapter describes the employed experimental method, named the electron beam evaporation technique to prepare of SiC_x thin films samples.

2.1 Overview of Deposition Techniques

Silicon carbide was naturally discovered in meteorites in 1824 by Jons Jacob Berzelius. Later on, in 1891 it was produced by American inventor Edouard G Acheson using sublimation method, while attempting to synthesis artificial diamonds. Hence, SiC_x films can be processed with sophisticated deposition techniques in both amorphous and crystalline forms [32] at low and high temperatures. The quality and crystal size of SiC material has been limited to the progress of the research technology. To increase interest, produce a good quality and growth large area of SiC material, the development of the deposition techniques is required.

A variety of deposition techniques have been employed to synthesis SiC_x thin films with different structures such as amorphous, microcrystalline and /or nanocrystalline, to determine the desired physical properties for particular applications. These techniques include a chemical and physical vapour deposition methods such as low pressure chemical vapour deposition (LPCVD), plasma enhanced chemical vapour deposition (PECVD), hot wire chemical vapour deposition (HWCVD), pulsed laser deposition (PLD), Molecular beam epitaxy (MBE), sputtering, and electron cyclotron resonance (ECR). All these techniques have advantages and disadvantages in preparation of SiC_x films. However, chemical vapour deposition (CVD) methods namely PECVD and HWCVD are the conventional methods. The advantage of these mentioned techniques is to yield SiC material with low defect concentration at low substrate temperature. Methane (CH_4) and silane (SiH_4) gases are routinely used as feed gas source to synthesis SiC_x films using the above techniques.

PECVD is the most commonly used method to prepare a-SiC$_x$:H films using pure CH$_4$ and SiH$_4$ gases in a hydrogen flow for mass production of thin silicon solar cells. However, this technique is subject to some limitations, due to problem of ion bombardment, high hydrogen content, low carbon efficiency and low efficiency of gas decomposition. Thus, a degradation in the thin films quality with low deposition rate [33] affects the device stability.

Hot Wire Chemical Vapour Deposition (HWCVD, also known as (Catalytic- CVD) has been successfully used for deposition of SiC$_x$ thin films at low substrate temperature below 400 ^{o}C with high deposition rate [10] and good quality films with large area uniformity are obtained for industrial production. Due to its simplicity, efficient cracking of the feedstock, lack of plasma-induced damage and replacement of plasma in PECVD by hot filament. The HWCVD offers an alternative for deposition of films with high deposition rate at low temperature of the substrate. HWCVD is described as an ion, electron and surface charge – bombardment free process, this results in strain-free films and the absence of powder in the deposition chamber. The uniformity of the resulting films allows also an easy interfacing with other layers. Moreover, a supply of high density of atomic hydrogen due to efficient decomposition of the gas on the heated filament; high hydrogen dilution in the feed gas induces crystallization of SiC$_x$ films.

However, the capability of the HWCVD to obtain device quality can be limited at very high temperature of the filament as the wire will start to evaporate and contaminate the growing film. Other techniques such as ECR, sputtering and LPCVD are less considered, due to many disadvantages ranging from non-uniform deposition over large area, porous and void-rich films, to high temperature of the substrate up to 900 ^{o}C [34, 35]. High temperature of the substrate is not only power consumption intensive but it limits the use of some substrates such as glass that start to sag and even melt in this T regime.

In large area production, the electron beam physical vapor deposition (e- beam PVD) was demonstrated as a substitutional deposition technique to plasma enhanced chemical vapor deposition, due to high deposition rates exceeding few micrometres per minutes [36, 37]. Furthermore, e-beam PVD requires less safety procedures. However, the e-beam technique provides low quality materials, which is characterizes by directional, non-conformal growth

with rough surfaces. In contrast to PECVD, which produces an omni-directional flux of material and therefore a nearly conformal coating on structured surfaces, e-beam PVD yields a directional deposition of thin film. At the start of this study, e-beam was the only deposition technique available to us. We have thus used it to grow SiC films with non-hydrogen dilution. Adopting low deposition rates and keeping the thickness of the grown layers thin (less than 300 nm), smooth and uniform films were obtained.

2.2 Electron Beam Physical Vapour Deposition (e-beam PVD)

The electron beam deposition is a physical vapor deposition method with high growth rate. This method was found appealing method for silicon thin film in photovoltaic applications [38]. The e- beam PVD method has been used earlier in 1970 by G. V. Bunton [39] to prepare silicon carbide SiC_x thin films on different substrates. The electron beam evaporation as physical vapour deposition technique is based on electrons bombardment to evaporate a target material. The working principle of this method consists in evaporating atoms from a target using an electron beam provided by a charged filament. The beam is focussed on the sample-target by a magnetic field. The evaporated atoms from the target impinge on the surface of the substrate and solidify to form a layer under low-pressure environment.

A schematic illustration of the electron beam evaporation technique is shown in fig 2.1. The chamber comprises the electron source, the crucible and substrate sections. A shutter is fitted to allow the operator to start, time the deposition and stop the deposition at the desired instant while the crystal monitor will record the deposited thickness. A heater can be fitted to bring the substrate at the desired temperature.
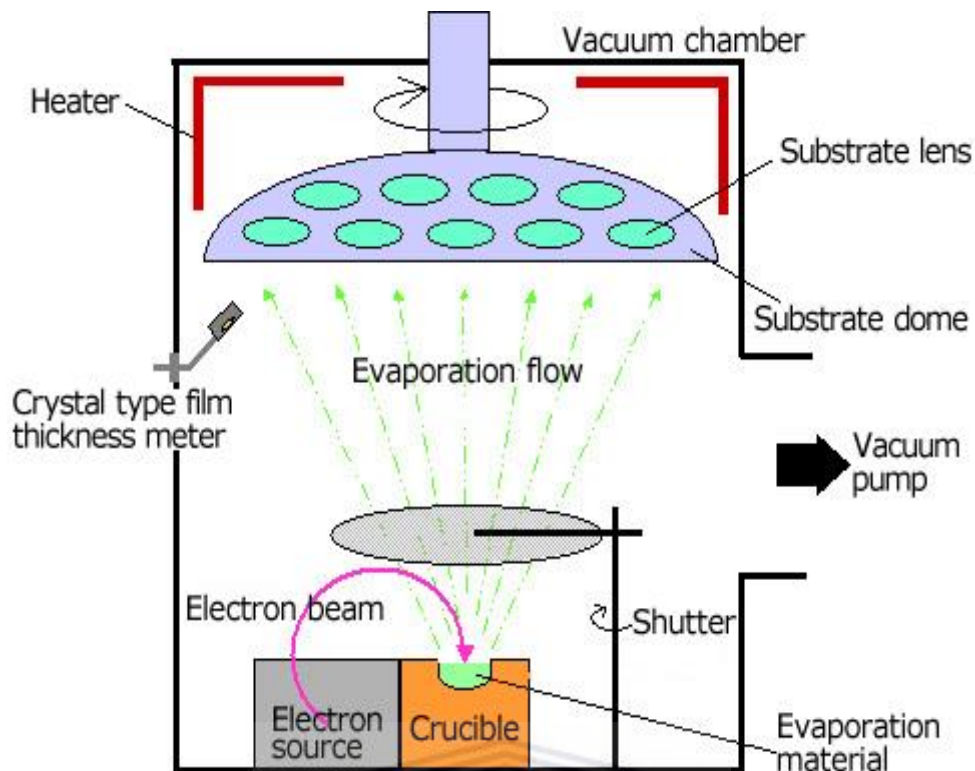
Figure 2.1: Schematic representation of an electron beam deposition chamber and evaporation material process [40].

2.3 SiC Thin Films Deposition

In this study, a corning glass (7059) and crystalline silicon (c-Si) <100> substrates of thickness (375μm) were utilized to prepare amorphous silicon carbide thin films. A diamond pen and tweezer were used to cut c-Si substrates into pieces of size 2 cm × 2 cm and handle the samples, respectively. Meanwhile, the glass plates were cut into 1 cm × 1 cm. The substrates were cleaned ultrasonically in bath of acetone and methanol in sequence of five minutes. Crystalline silicon substrates were thereafter dipped in a solution of 5% Hydrofluoric acid (HF) for one minute to remove the native surface oxide. Further, the substrates were rinsed in de-ionized water and dried. Finally, those substrates were mounted in load-lock chamber of the deposition chamber.

12

For this study, the deposition of SiC_x thin films was conducted in the material research department at iThemba Labs, Cape Town. In the evaporation system, a high purity commercial hot pressed SiC sheet of 99.99% is used as target material and placed on a refractory Tungsten crucible. Prior to deposition, the e-beam PVD chamber was evacuated to a base pressure of ~ 7. 9 $\times 10^{-6}$ mbar. The generated electron beam generated was accelerated in a high voltage, therefore that on impact with the target source, it will impart sufficient energy to evaporate the material. No heating was applied to the substrate, hence that the temperature of the substrate can be assumed far too lower than the melting point of the depositing species; in such case the evaporated atoms condense on the surface of the substrate. A typical deposition rate of 0.6 Å/s was maintained and the time of deposition was varied according to the desired thickness. The thickness was estimated by a quartz crystal monitor. After deposition, the samples were left under vacuum to avoid oxidation. They were thereafter removed from the chamber and prepared for thermal annealing process in a dedicated ceramic tube.

2.4 Annealing Procedure

Annealing of samples can be used for two main purposes; induce the microstructure change and phase transformations of the as-deposited SiC_x thin films. The SiC_x thin films are subjected to annealing at high temperature to cause rearrangement of the structure of the bonds and to enhance the recrystallization. Numerous experiments have established that annealing of the deposited thin films causes the alteration of its physical properties and induce the formation of the nanoclusters embedded in amorphous SiC matrix [41, 42]. Depending on the available energy at the annealing temperature, Si and C atoms can break away from their previous bonding and rearrange in much more favourable sites of lower energy and thus the network crystallize in the process. For instance, Matthias [43] showed that the formation of Si and SiC nanocrystals in amorphous SiC matrix can be induced by annealing at a threshold temperature of 900 ºC However, the crystallization of SiC nanocluster was only observed at higher temperatures in excess.

The samples previously deposited onto c-Si were subjected to different temperatures of anneal under vacuum, in the range between 500 ºC and 1000 ºC for a duration of 1 hour each time in Ar gas atmosphere. A dedicated cleaned ceramic tube was used. The temperature was ramped from RT to the desired temperature of annealing at a constant rate of 10 ºC per minute.

13

Thereafter the samples were cooled naturally overnight back to room temperature. Then, samples on c-Si substrates were utilized for FTIR, RS, XRD, SEM, and EDX measurements. While samples on glass substrate were used for XRD and optical characterization through UV-VIS-NIR measurements.

CHAPTER 3

Analytical Techniques

Accurate and comprehensive techniques are required to characterize silicon carbide thin films. This chapter reviews the fundamentals of various analytical techniques needed for study the structural and optical properties of SiC_x thin films. Table 3.1 lists the analytical techniques used in this study.

Table 3. 1: The analytical techniques used in this study.

Technique	Study
Fourier Transform Infrared Spectroscopy (FTIR)	Chemical bonding
Raman Spectroscopy (RS)	Structural phase
X-ray diffraction (XRD)	Crystalline phase
Scanning Electron Microscopy (SEM)	Surface morphology
Energy dispersive X-ray Spectrometry (EDX)	Elemental composition
Ultraviolet-Visible-Near-infrared (UV-VIS-NIR)	Optical analysis

3.1 Structural Analysis

It is important to understand the structural properties of SiC_x thin films in order to optimize the material and implement it in technological applications. Furthermore, understanding the correlation between structural to optical properties is necessary for the photovoltaic technology. Various conditions in the deposition process can influence a large variation in the structural properties of the thin films. The determination of the structural properties plays an important role in thin film photovoltaic technology. Several analytical techniques were developed to study the structure of matter. The complementary techniques used for structure analysis of the samples includes Fourier Transform infrared (FTIR) and Raman (RS) spectroscopies, to provide information on the nature of the chemical bonds within SiC_x thin films and to estimate the density of the vibrational /rotational bonds. Other techniques such as XRD, SEM/EDX are used to study the structure of crystalline solids and surface morphology / elemental composition, respectively.

The next sections present the fundamentals of these techniques selected to perform the structural characterization of SiC_x samples investigated in this study.

3.2 Fourier Transform Infrared Spectroscopy (FTIR)

Fourier Transform Infrared (FTIR) spectroscopy is one of the most important analytical techniques used for structure analysis in solid state when vibrational modes are involved. It is a non-destructive technique that requires little or no sample preparation, that provides vital information on molecular chemical bonding. The measurements are easy and fast to perform but FTIR is only sensitive to asymmetric molecular bonds.

As the name suggests, FTIR spectroscopy deals with interaction of electromagnetic radiation in the infrared region of the spectrum with matter, by displaying the absorption bands in the incident IR spectrum. In molecular vibrational spectroscopy, a change in the electric dipole moment must occur for the IR vibrational mode to be active. IR spectra can be used to identify the functional groups according to their vibrational frequencies. Not only FTIR gives valuable

16

qualitative chemical analysis of bonding structure of SiC_x films, but it also gives quantitative analysis about the content of silicon carbide bonds in different modes.

3.2.1 Molecular Vibration

When an IR radiation passes through a sample, absorbs photons of IR radiation at a specific frequency. This absorption process occurs when there is a match between the resonant vibrational frequency of the molecule and the electric field frequency of the radiation. Interaction of the IR radiation with the molecules causes a change in its dipole moment due to transitions in vibrational states [44]. Like in electronic states between band to band transitions in the electronic cloud of atoms, molecular vibrational energy states are also discrete. Consequently, an absorption peak appears at a particular frequency which determines the energy absorbed. The resultant characteristic IR spectrum, indicates the absorbed frequencies, most of the time absorption bands instead, and since each vibrational mode will have its unique energy, vibrational frequencies / bands act as molecular fingerprints.

The frequency of a vibrating molecule in the IR region of the spectrum is expressed as:

$$\nu = \frac{c}{\lambda} \tag{3.1}$$

It is however, customary to report FTIR data in terms of wavenumber [45]:

$$\tilde{\nu} = \frac{\nu}{c} = \frac{1}{\lambda} \tag{3.2}$$

It follows that the wavenumber is directly proportional to the energy difference between quantized states i.e. it is directly proportional to the energy of transition:

$$\Delta E = hc\tilde{\nu} \tag{3.3}$$

17

Where,

$\tilde{v}$ = wavenumber

λ = wavelength

c = speed of light

A classical treatment of the vibrating diatomic molecule can simplify the motion as one single particle with a reduced mass µ oscillating back and forth from a position of equilibrium; the wavenumber is thus linked to the force constant k and the reduced mass µ as [45, 46]:

$$\tilde{v} = \frac{1}{2\pi c} \sqrt{\frac{K}{\mu}} \qquad (3.4)$$

This relationship is derived from Hooke's law. The constant k is the force constant which varies from one bond to another, and µ is the reduced mass of the bonded atoms, which can be expressed as:

$$\mu = \frac{m_1 \, m_2}{m_1 + m_2} \qquad (3.5)$$

Molecular vibrations of asymmetrical molecules such as Si-C or Si-O, causes a change in the dipole moment. This change leads to the stretching and bending vibrations of the IR-active bonds. Whereas, the vibration of symmetric molecules such as Si-Si, C-C do not change the dipole moment, and cannot absorb infrared radiation. FTIR is not thus a good tool to analyse symmetric molecular vibrations.

3.2.2 Modes of Vibrations

Transitions between vibrational energy states correspond to selected frequencies. These vibrational frequencies lead to different vibrational modes caused by movement of atoms in the molecule. Such vibrations can be in or out of plane. Stretching and bending movements result in vibration modes of molecule that are infrared active. In a polyatomic molecule consisting of N number of atoms, as each atom can move in three direction x, y and z, this

implies 3N degrees of freedom. This number include however three translational motions of the molecule along the three axes and three rotational motions of the molecule about the three axes of rotation intersecting its centre of gravity; this reduces to 3N-6 for nonlinear molecule. For a linear molecule, as it cannot rotate about the molecular axis, only 3N-5 normal vibrations are retained. Fig 3.1 illustrates different vibration modes associated with a) linear molecule CO_2 of two stretching modes symmetric for in-phase and asymmetric for out of phase, b) nonlinear molecule H_2O of two stretching modes and one bending.

a) Linear molecule CO_2 b) Nonlinear molecule H_2O
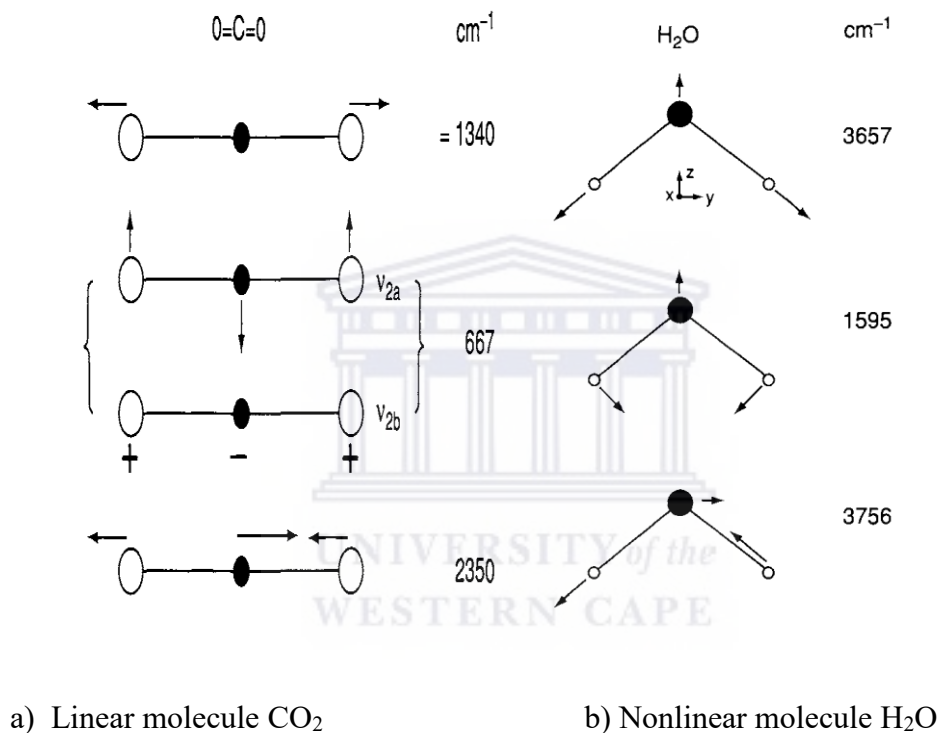
Figure 3.1: Normal modes of vibration for a) linear molecule (CO_2) and b) nonlinear molecule (H_2O) [47].

3.2.3 The Content of Silicon Carbide Bonds

As mentioned above, FTIR is sensitive only to asymmetric bonds. FTIR will thus a technique of choice to analyse SiC_x and SiO_x bonds that are most of the time found in the SiC_x matrix. In the wavenumber studied ~400 cm^{-1} to ~1200 cm^{-1}, different vibrations modes are noted such as Si-C stretching mode at 800 cm^{-1} and Si-O stretching mode at 1100 cm^{-1}. The integrated

19

intensity of the absorption band in the FTIR spectrum allows to determine the total content of the vibrating bonds [48]:

$$I = \int \frac{\alpha(\omega)}{\omega} \, d\omega$$ (3.6)

Where $\alpha(\omega)$ is the absorption coefficient and ω is the wavenumber. For non-hydrogenated SiC_x films, the integration of the band centered around 800 cm⁻¹ allows to estimate Si-C bond concentration, while that centered around 1100 cm⁻¹ allows the estimation of Si-O bond density following:

$$N = A_\omega \times I_\omega$$ (3.7)

Where A_ω represents the absorption – cross section which is 2.13×10^{19} cm⁻² and 1.5×10^{19} m⁻² for Si-C and Si-O bands, respectively [43, 49]. The concentration of carbon in the samples from FTIR is calculated by the following equation:

$$C_c = \frac{N_{si-c}}{N_{si} + N_{si-c}} \times 100 \, \%$$ (3.8)

Where N_{si-c} is represents the bond density of SiC_x which can be found by applying the formula above and N_{Si} is the bond density of silicon atoms, which is equal to 5×10^{22} cm⁻³.

In order to compare the absorbance of a same mode in different films often of different thicknesses; it is important to convert the measured transmittance to absorption coefficient which is independent of the thickness travelled Brodsky *et al.* [50] proposed a relation that links the interference free transmittance T to both the absorption coefficient α and the thickness of the film d:

20

$$T = \frac{4T_0^2 e^{-\alpha d}}{(1 + T_0)^2 - (1 - T_0)^2 e^{-2\alpha d}} \tag{3.9}$$

Where d is the thickness of the film, $T_0 = 0.54$, a theoretical value of the transmissivity of the c-Si substrate in the absorption free region of the spectrum i.e. where its absorption coefficient is zero.

It is important to stress the expression of T above in relation (3.9) has been derived assuming $n_{sub} = n_{film} = 3.42$, thus for a film of crystalline Si on a thick c-Si substrate. To minimize errors, one should measure experimentally the specific value of T_o the film one wants to determine the absorption coefficient.

The relation (3.9) can be solved for α in terms of the measured T. The calculated values are generally accurate for values of $\omega d > 0.06$ [51]; otherwise a correction suggested by Maley *et al.* [51] must be applied:

$$\alpha_{TRUE} = \frac{\alpha_{BCC}}{1.72 - 12\,\omega d} \quad ,for\ \omega d \leq 0.06 \tag{3.10}$$

$$\alpha_{TRUE} = \alpha_{BCC} \quad ,for\ \omega d > 0.06 \tag{3.11}$$

3.2.4 Experimental Set-up

FTIR is a sensitive analytical technique to asymmetric bonding in materials. It was used to identify the chemical bonds present in SiC_x material depending on the film composition. Fourier transform infrared (FTIR) spectroscopic investigation was done using a Perkin-Elmer Pentagon 1000 FTIR spectrophotometer in the wavenumber's range between 4000 cm^{-1} and

400 cm^{-1} with a resolution of 4 cm^{-1}. The film transmission was normalized by subtracting the reference spectrum from that of the film on the c-Si substrate.

3.3 Raman Spectroscopy (RS)

Raman spectroscopy is a complementary technique to FTIR for molecular vibrations characterization. It is used for investigation in the chemical structure, stress and crystallinity in samples [52]. While in IR spectroscopy, the absorption of IR light in the sample as function of wavenumber is measured, in Raman spectroscopy the scattered signal is measured. Both the strong Rayleigh elastically scattered and the weak Raman inelastically scattered beams are detected. The basic fundamentals of Raman spectroscopy are presented in the next subsection.

3.3.1 The Fundamentals of Raman Spectroscopy

The radiation intensity falling on a semi-transparent sample is reflected on the surface and other interfaces, absorbed through the sample and the remaining intensity is transmitted. The three phenomena are usually quantified in terms of Reflectivity (R), Absorptivity (A) and Transmittivity (T), respectively. The absorption process is quite complex; true absorption is realized through the absorption of photons whose energy matches the difference between the ground and excited state's energies of the molecule. Photons can however also scattered from impurities, defects and other inhomogeneities that cause the variation of the refractive index in the matrix material on a length scale smaller than the wavelength of the light [53]. This process redirects the electromagnetic radiation from its original path and thus contribute to overall absorptivity. The scattering cross-section varies with the wavelength as [53]:

$$\sigma_s(\lambda) \sim \frac{1}{\lambda^4} \qquad\qquad (3.12)$$

As the Rayleigh scattering occurs when the scattering centres are very small compared to the wavelength of the radiation, it is the strongest in intensity and inhomogeneities materials tend to scatter more strongly shorter than longer wavelengths.

22

Raman lines (molecular vibrational frequencies) appear normally in the UV-visible region and thus the excitation (practically a monochromatic laser) will be also chosen in the UV-visible. The electric field strength's fluctuation with time is written:

$$E = E_0 \cos 2\pi v_0 t \tag{3.13}$$

where E_0 and v_0 are the maximum field amplitude and the frequency of the laser, respectively. Suppose a diatomic molecule is irradiated; the positively charged nuclei and the negatively charged electron clouds are accelerated in two different directions by the electric field; this causes the separation of the charge centres and thus an electric dipole moment μ is induced:

$$\mu = \alpha E = \alpha E_0 cos 2\pi v_0 t \tag{3.14}$$

where α is the proportionality constant called polarizability. If the molecule is vibrating with a frequency v_m, the nuclear displacement is q is written:

$$q = q_0 cos 2\pi v_m t \tag{3.15}$$

where q_0 is the maximum vibrational amplitude. For a small amplitude of vibration, α is a linear function of q [47]:

$$\alpha = \alpha_0 + \left(\frac{\partial \alpha}{\partial q}\right)_0 q_0 + \cdots \tag{3.16}$$

Where α_0 and $\left(\frac{\partial \alpha}{\partial q}\right)_0$ are the polarizability and the rate of change of α with respect to the change of q, evaluated at the equilibrium position, respectively. The combination of the three relations above yields [47]:

23

$$\mu = \alpha_0 E_0 cos2\pi\nu_0 t + \frac{1}{2}\left(\frac{\partial\alpha}{\partial q}\right)_0 q_0 E_0 [cos\{2\pi(\nu_0 + \nu_m)t\} + cos\{2\pi(\nu_0 - \nu_m)t\}] \qquad (3.17)$$

The first term represents an oscillating dipole radiating light at the exact frequency of the radiation or Raleigh scattering while the second corresponds to Raman scattering at a frequency $(\nu_0 + \nu_m)$ for anti-Stokes and $(\nu_0 - \nu_m)$ for Stokes; in the anti-Stokes, a phonon is annihilated i.e. the molecule was in a virtual excited state on the absorption of the laser (less probabilistic and thus low intensity Raman signal) while in the Stokes, a phonon is created i.e. the molecule was in the ground state on the absorption of the laser, this is more likely and thus the Stokes will be more intense. It is clear that for the vibration to be Raman active, $\left(\frac{\partial\alpha}{\partial q}\right)_0$ must be different of zero i.e. the rate of change of the polarizability with the vibration must be not zero. It must be also be pointed out that the Raman spectrum measures ν_m i.e. the shift frequency from the Raleigh. It is then understood that the Raman effect is an inelastic process; fig 3.2 contrasts the IR absorption, the Raleigh (R) scattering, the Stokes (S) and anti-Stokes (A) Raman.
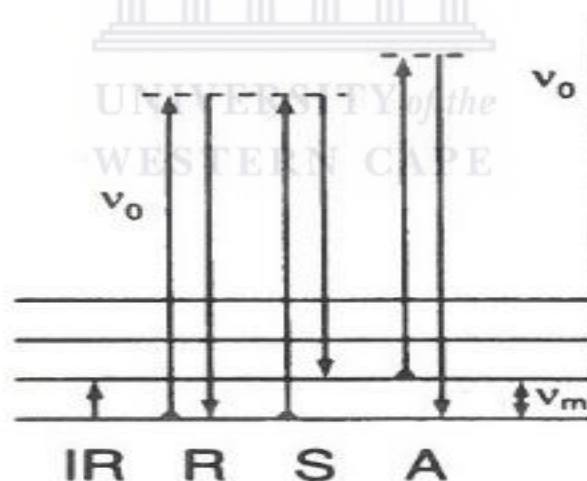
Figure 3.2: Infrared and normal Raman vibrational processes [47].

Inelastic scattering resulting in phonons, is subdivided into optical and acoustic phonons [53]; the first represents frequencies occurring in the optical spectral region (infrared or Raman) and the second, as the name indicates, occurs in the sonic and ultrasonic region. The dispersion formula describing both gives a frequency function dependent on the masses of the particles in

24

the crystal lattice, force constant, the distance between the masses in the unit cell and their reduced mass. Stokes and anti-Stokes scattering must conserve both energy and momentum as shown in fig 3.3.
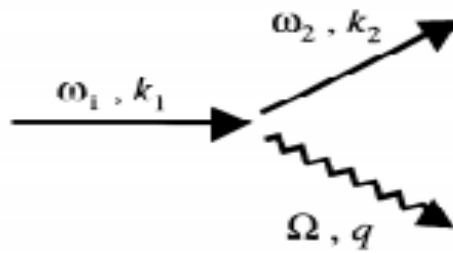
Figure 3.3: The stokes and anti-stokes process of inelastic scattering [53].

The fig 3.3 illustrates the interaction process of inelastic scattering involved in the stokes and anti-stokes scattering processes. In the process, light incident with frequency ω_1 and wave vector k_1 is scattered against a lattice vibration generating or annihilating a phonon of frequency Ω and wave vector q. The scattered photon has frequency ω_2 and wave vector k_2.

The conservation of energy during the interaction requires that:

$$\omega_1 = \omega_2 \pm \Omega \tag{3.18}$$

and the conservation of momentum gives:

$$k_1 = k_2 \pm q \tag{3.19}$$

The signs + in the two equations above correspond to phonon emission (anti-stokes scattering), while the – signs correspond to phonon absorption (scattering). Thus, the light is shifted down in frequency during a stokes process and up in frequency in an anti-stokes event.

The difference between infrared absorption and Raman scattering can be observed in fig 3.2. As stated, IR absorption would involve direct excitation of the molecule from one state to another state by a photon of exactly the energy difference between them. In contrast, Raman scattering uses much higher energy radiation and measures the difference in energy between two states by subtracting the energy of the scattered photon from that of the incident beam for Stokes mode or adding this difference to that of the incident beam for anti-Stokes mode; the last is seldom used as mentioned earlier.

Intense Raman scattering occurs from vibrations which cause a change in the polarizability of the electron cloud around the molecule. Usually, symmetric vibrations cause the largest changes and give the greatest scattering. This contrasts with IR absorption where the most intense absorption is caused by a change in dipole moment due to asymmetric vibrations. As result the two techniques are often complementary and when used together, they give a better view of the vibrational structure of a molecule.

3.3.2 Experimental Set-Up

Raman was performed in the range $300 - 1600$ cm^{-1} using a 532 nm green laser line with an excitation power of 1.05 mW. The Raman scattered light was recorded by a CCD detector cooled down to -131 $^{\circ}$C.

3.4 X-Ray Diffraction (XRD)

X-ray diffraction (XRD) is a probing technique used for crystal structure analysis. It is employed to study the crystallinity, crystal orientation of the materials and to evaluate the crystal size and residual stresses. The technique is based on the diffraction of X-rays, a form of electromagnetic radiation of high energies and thus short wavelengths that are in the order of interatomic spacing for solids; for this reason, XRD is widely used for atomic interplanar distances and crystal structures in solids.

3.4.1 Absorption of X-rays

When X-rays interact with matter, part of the absorbed intensity is transmitted while another part is absorbed. The decrease in intensity as the X-rays beam travels through a homogeneous sample can be written:

$$- \frac{dI}{I} = \mu \, dx \qquad (3.20)$$

where μ is the linear absorption coefficient of the substance. By integration of the equation above is solved as:

$$I = I_0 \, e^{-\mu x} \qquad (3.21)$$

Where I_0 is intensity of incident x-ray beam and I is the remaining intensity after the beam has travelled a thickness x in the layer. The quantity μ/ρ is a constant of the material and called the mass absorption coefficient, since the linear absorption coefficient μ is proportional to the density ρ. Then, the equation above can be written as:

$$I = I_0 \, e^{-(\mu/\rho)} \qquad (3.22)$$

If the substance is a mixture or a chemical compound containing more than one element, its mass absorption will be the weighted average of the mass absorption coefficient of its constituent elements as follow:

$$\frac{\mu}{\rho} = \omega_1 \left(\frac{\mu}{\rho}\right)_1 + \omega_2 \left(\frac{\mu}{\rho}\right)_2 + \cdots \qquad (3.23)$$

27

where ω_1, ω_2, etc, are the weight fractions of elements 1, 2, etc, in the substance and $\left(\frac{\mu}{\rho}\right)_1$, $\left(\frac{\mu}{\rho}\right)_2$, etc, their mass absorptions.

3.4.2 Diffraction Techniques Using X-Rays

Diffraction occurrence in XRD follows from the periodicity of the crystals; one thus measures the phase relationships arising from X-rays waves that have been scattered regularly spaced planes in the crystals. When in-phase X-ray radiation of wavelength λ is incident on parallel planes with interplanar spacing d_{hkl} at an angle θ, the condition for constructive interference is given by the well-known Bragg law as [54]:

$$n\lambda = 2\, d\, sin\, \theta_B \qquad (3.24)$$

where n represents the order of diffraction. The interplanar spacing of two adjacent plane is linked to the lattice parameters and the Miller indices; for crystals structures that have cubic symmetry for instance, we have [54]:

$$d_{hkl} = \frac{a}{\sqrt{h^2 + k^2 + l^2}} \qquad (3.25)$$

The broadening of the diffraction peak β can be used to calculate the crystal size *t* using the Scherer formula [55]:

$$t = \frac{0.9\lambda}{B\, cos\, \theta_B} \qquad (3.26)$$

28

For accurate estimation of the crystal size, the observed peak broadening from XRD peak must be corrected from the instrument broadening at the relevant 2θ angles. If the crystal is under strain, a full treatment should include the strain component in the total used broadening [56]:

$$\beta_e = 2\ \varepsilon tan\theta \qquad\qquad (3.27)$$

β_e is the strain broadening which is dependent of the diffraction angle and ε is the strain.

3.4.3 Experimental Set-Up

XRD measurements of SiC_x thin films were recorded using a diffractometer with an X-ray source of Cu Kα (λ=1.5418 Å) and the diffracted intensities were recorded in the range of 2θ =10-70° with a step size of 0.034° on samples as- deposited on glass substrates and as- annealed to investigate both phases and crystallinity in the films.

3.5 Scanning Electron Microscopy (SEM)

In scanning electron microscopy, a surface of a specimen is scanned by an electron beam and the inelastically backscattered beam of electrons from the surface of the sample is imaged and magnified. SEM provides thus information on the surface morphology of the specimen. Magnifications in excess of 50000 times can be achieved in high resolution (HR) SEM. At the same time the energies of the secondary scattered electrons can be collected by a separate detector and this provides valuable information on the elemental composition of the sample.

3.5.1 Theory

Microscopy is a technique that uses a set of optics to image a small object into a magnified image. Hence, scanning electron microscopy is an imaging system to magnify tiny objects by using a beam of electrons instead of electromagnetic light. It is primarily used for studying the surfaces, or near surface structure of bulk specimens. The basic principles applied for scanning electron microscopy is the similar as those applied for light microscopy [57]. The important

concepts in SEM to be dealt with are the resolution, magnification, depth of field, and lens aberration.

Fig. 3.4 displays a schematic of the main components of a SEM instrument; the electron gun consisting commonly of a thermionic tungsten filament. The electrons are accelerated in a potential difference ranging between 1 kV and 30 kV depending on the intended resolution. The beam passes through a set of lenses, scan coils and a narrow slit before hitting the specimen from which secondary electrons will be generated and imaged [57].
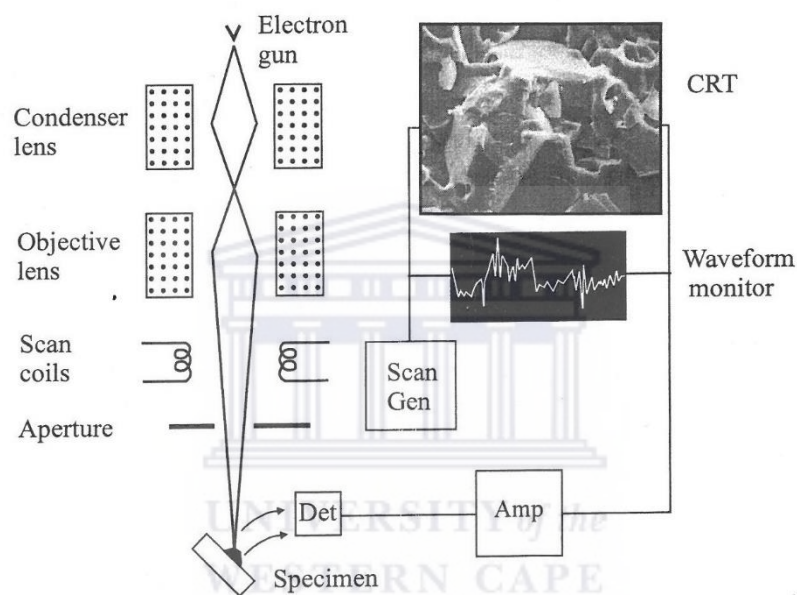

Figure 3.4: The main components of a scanning electron microscopy [57].

Fine beam of electrons is scanned across the specimen by scan coils while a detector counts the number of low energy secondary electrons or inelastically scattered backscattered electrons from each point of the surfaces. At the same time, the spot of a monitor is scanned while the brightness of the spot is modulated by the amplified current from the detector. Consequently, the mechanism by which magnification is defined in the SEM is simple and involves no lenses. The raster scanned by the electron beam on the specimen is far smaller than the raster displayed on the screen. The linear magnification is then defined as the side length of the screen (L) divided by the side length of the raster on the specimen (l).

3.5.2 SEM Signals

When the electrons interact with a specimen, the energy of the incident photons is dissipated with emission of secondary electrons and backscatter of the inelastic scattered electrons. The main principle of scanning electrons microscopy is to detect secondary electrons and backscattered electrons through an inelastic scattering process. Fig 3.5 displayed the region into which electrons penetrate the specimen surface is known as the interaction volume. X-ray are not easily absorbed and hence forms the major component of the interaction volume, which may be several micrometres in diameter. Backscattered electrons originated from a much smaller volume compared to x-ray and therefore will give information at a much higher spatial resolution compared to X-rays. The secondary electrons are generated by both primary and backscattered electrons, but are emitted from a region which is comparable to the beam diameter. As such, the secondary electrons signal in the SEM gives the highest spatial resolution.
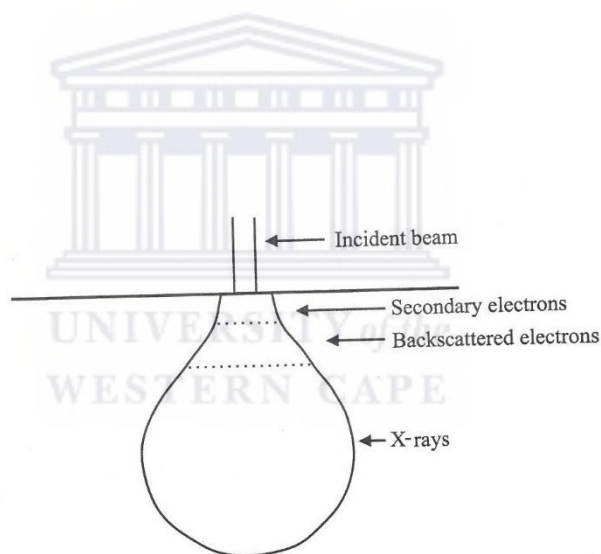
Figure 3.5: The region where the electrons scattered in the specimen into secondary, backscattered, and X-rays electrons [57].

A variety of signals are produced from sample and observed using sensors as shown in fig 3.6, due to penetrate the surface of sample by focused beam of electrons. Thus, the information relates to the specimen surface can be determined with lower energy of secondary electrons.
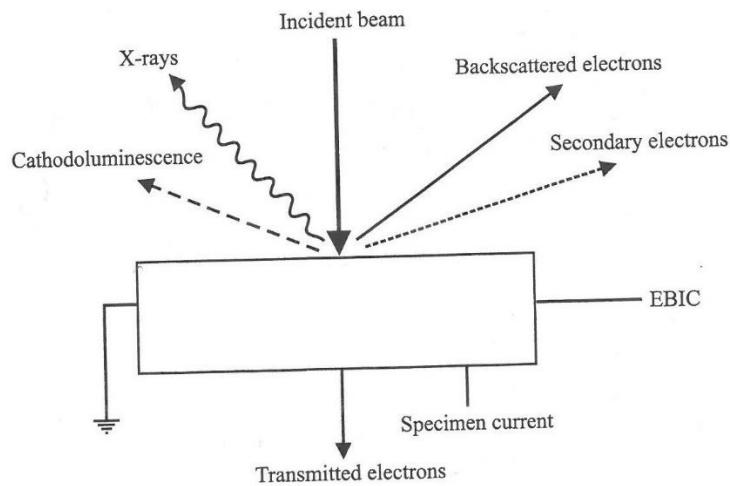
Figure 3.6: The signals used in the scanning electron microscope [57]**.**

Detecting secondary electrons by use a scintillator-photomultiplier system known as the Everhart-Thornley. The secondary electrons strike a scintillator which then emits light. Photons are then transmitted down a light pipe into a photon-multiplier. Photon-multiplier then converts photons into pulses of electrons which may then be amplified and used to be modulate the intensity of the screen. While, backscattered electrons which are travelling in the appropriate direction to hit the scintillator of the Everhart-Thornley detector.

3.5.3 Experimental Set-Up

In this study, the surface morphology and elemental composition of the films were examined using a Zeiss Auriga field-emission gun scanning electron microscopy (FEG-SEM) operated at 40 keV for imaging using an Everhart-Thornley secondary electron detector. EDX measurements were done to analyze the chemical composition; for this effect, an Oxford Instruments X-Max solid-state silicon drift detector was used to collect the spectra.

32

3.6 Optical Analysis

Optical analysis consists in studying the response of matter to external electromagnetic radiation. This response is expressed in terms of the dielectric constant (ε_r) for non-magnetic materials as it is the case for semiconductors. As the refractive index (n) is directly linked to the dielectric constant, the knowledge of one of them gives a good description of the optical response of the material under study. SiC materials are desirable for their wide band gap; it happens also that the band gap of SiC_x films can be tuned over a wide range depending on the deposition conditions and the resultant structural properties of the material thereof. In particular the complex refractive whose real part n and the imaginary part κ (directly linked to the absorption coefficient) can be determined from the measured transmission and reflection spectra. As the band gap is extrapolated from the absorption coefficient, the optical analysis is necessary characterisation tool of SiC_x thin films.

Depending on the sought application for SiC_x films, one will need to preserve a good passivated amorphous tissue for enhanced absorption coefficient or then bring the deposited SiC_x films to near stoichiometric microstructure for high band gap of the material. The annealing at varied temperatures has been a method adopted in this study to tune the stoichiometry of as deposited films; thus the correlation of optical constants with annealing is an important step to understand the behaviour of the material.

This section presents a short explanation of the optical spectroscopy. In addition, the section presents an overview of the applied theory including the basics of the electromagnetic theory, concepts of dielectric functions models and of the optical band gap.

3.6.1 Ultraviolet-Visible-Near Spectroscopy (UV-VIS-NIR)

The Ultraviolet-Visible-Near Infrared Spectroscopy is used widely for the study the optical analysis of materials. The measurements of T / R spectra are very simple and non-destructive. A compact spectrophotometer covering the range from 200 nm - 1800 nm is sufficient; modular set-ups comprising a spectrometer, deuterium and halogen sources of light, a set of optic fibres and necessary lenses can as well be used as in the current study.

Although the collection of transmission and reflection data T(λ) and R(λ) respectively, is straightforward, their processing requires a good understanding of both electron interband processes and dielectric effective medium approximation theories. For homogeneous Si based thin films displaying enough interference patterns in the visible region, the Swanepoel method [58]–[60] has been successful in determining the optical constants from the T(λ) alone; this thesis will not expand further on the subject. Instead for non-homogeneous thin films or composite systems where the dielectric constants are continuously varying, dielectric effective medium approximation is required; this thesis will expand on the existing models used in the scout [61].

3.6.2 Light –Matter Interaction Theory

Assuming an isotropic material and neglecting non-linear optics effects, the microscopic response of the material to the electric field is primarily determine by the polarization P [53], which tends to align the microscopic dipoles along the field:

$$P = \varepsilon_0 \chi E \qquad (3.28)$$

ε_0 and χ are the permittivity of vacuum and the electric susceptibility of the medium respectively. The polarisation is the additional term above that of the response to the electric field of a dipole in vacuum; this is expressed in term of the vector displacement D:

$$D = \varepsilon_0 E + P \qquad (3.29)$$

The total displacement of a medium can thus be expressed in terms of the relative dielectric constant of the medium ε_r as:

34

$$D = \varepsilon_0 \varepsilon_r E \qquad (3.30)$$

where

$$\varepsilon_r = 1 + \chi \qquad (3.31)$$

Similarly, the magnetic flux density B in the presence of a magnetic material is related to the magnetic field strength H as:

$$B = \mu_0 \mu_r H \qquad (3.32)$$

where μ_0 and μ_r are the magnetic permeability of vacuum and the relative magnetic permeability of the medium, respectively.

A similar expression to the link between the relative dielectric and electric susceptibility is written between the relative permeability and the magnetic susceptibility:

$$\mu_r = 1 + \chi_M \qquad (3.33)$$

Maxwell's equations give a combined electric and magnetic response of a medium [53]:

$$\begin{cases} \nabla . D = \varrho \\ \nabla . B = 0 \\ \nabla \times E = -\dfrac{\partial B}{\partial t} \\ \nabla \times H = j + \dfrac{\partial D}{\partial t} \end{cases} \qquad (3.34)$$

ϱ is the free charge density and j is the current density. From the treatment of Maxwell's equations, it is shown that [53]:

$$\partial^2 E = \mu_0 \mu_r \varepsilon_0 \varepsilon_r \frac{\partial^2 E}{\partial^2 t} \qquad (3.35)$$

This expression has the same form as the wave equation, thus the phase velocity of electromagnetic waves can be written:

$$\frac{1}{v^2} = \mu_0 \mu_r \varepsilon_0 \varepsilon_r \qquad (3.36)$$

It follows that:

$$v = \frac{1}{\sqrt{\varepsilon_r \mu_r}} c \qquad (3.37)$$

The solution of the partial differential equation describing the wave equation above is written:

$$E(z,t) = E_0 e^{i(kz - \omega t)} \qquad (3.38)$$

Since, the refractive index is per definition the ratio:

$$n = \frac{c}{v} \qquad (3.39)$$

and that at optical frequencies $\mu_r = 1$; it follows that:

$$n = \sqrt{\varepsilon_r} \qquad (3.40)$$

As the wavenumber k is written:

36

$$k = \frac{n\omega}{c} \tag{3.41}$$

Using the definition of the current density;

$$j = \sigma E \tag{3.42}$$

The fourth of the Maxwell's equations listed above can be written [53]:

$$\nabla^2 E = \sigma \mu_0 \mu_r \frac{\partial E}{\partial t} + \mu_0 \mu_r \varepsilon_0 \varepsilon_r \frac{\partial^2 E}{\partial t^2} \tag{3.43}$$

Substituting the expression of E in the above expression, it is easy to see that:

$$k^2 = i\sigma \mu_0 \mu_r \omega + \mu_0 \mu_r \varepsilon_0 \varepsilon_r \omega^2 \tag{3.44}$$

As, k is complex, n is also complex and it is written as:

$$\tilde{n}^2 = \frac{\mu_r \sigma}{\varepsilon_0 \omega} i + \mu_r \varepsilon_r \tag{3.45}$$

The real part n determines the phase velocity and the imaginary part κ gives the extinction coefficient:

$$\tilde{n} = n + i\kappa \tag{3.46}$$

The wave propagating in the z direction in a medium of complex refractive index $\tilde{n}$ is thus described by:

$$E(z,t) = E_0 e^{i(\omega \tilde{n} z/c - \omega t)} = E_0 e^{-\kappa \omega z/c} e^{i(\omega n z/c - \omega t)} \quad (3.47)$$

It is clear that for non-zero extinction coefficient, the amplitude of the wave exponentially decays in the medium. In terms of intensity $I \sim E{\times}E^*$; one can relate to the absorption coefficient α by comparing I to the well-known Beer's law:

$$I(z) = I_0 e^{-\alpha z} \quad (3.48)$$

 It follows that:

$$\alpha = \frac{2\kappa\omega}{c} = \frac{4\pi\kappa}{\lambda} \quad (3.49)$$

In the microscopic models, $\tilde{n} \; and \; \tilde{\varepsilon_r}$ are not independent; their real and imaginary parts are related as :

$$\begin{cases} \varepsilon_1 = n^2 - \kappa^2 \\ \varepsilon_2 = 2n\kappa \end{cases} \quad (3.50)$$

For a weakly absorbing medium, we can thus simply the relations to:

$$\begin{aligned} n &= \sqrt{\varepsilon_1} \\ \kappa &= \frac{\varepsilon_2}{2n} \end{aligned} \quad (3.51)$$

If there is significant absorption, the real and imaginary parts extended expressions are used [53]:

$$\begin{cases} n = \dfrac{1}{\sqrt{2}}\left(\varepsilon_1 + (\varepsilon_1^2 + \varepsilon_2^2)^{1/2}\right)^{1/2} \\ \kappa = \dfrac{1}{\sqrt{2}}\left(-\varepsilon_1 + (\varepsilon_1^2 + \varepsilon_2^2)^{1/2}\right)^{1/2} \end{cases} \qquad (3.52)$$

It has to be mentioned also that the reflectivity R depends on both n and κ as [53].

$$R = \left|\frac{\tilde{n}-1}{\tilde{n}+1}\right|^2 = \frac{(n-1)^2 + \kappa^2}{(n+1)^2 + \kappa^2} \qquad (3.53)$$

### 3.6.3 Optical Modelling of Dielectric Functions

The optical functions are important to understand the optical behaviour of any solid material. For determining the optical functions, different computational methods were developed for extracting these functions [62,63]. These methods allow to correlate the optical properties of the materials to the structure of the network. Transmission and reflection spectra collected in the region of the EM spectrum spanning from the UV to the NIR are used for simulation using theoretical established optical functions.

The transmission spectrum is modelled as originating from a thin film deposited onto an infinite transparent substrate. Similarly, the reflection spectrum is obtained from interference of waves reflecting from the surface and the interface of thin film deposited onto an infinite substrate. Fig 3.7 shows a schematic of the mechanism of how the reflection spectrum is generated from the boundaries of a thin film over a finite substrate.

39
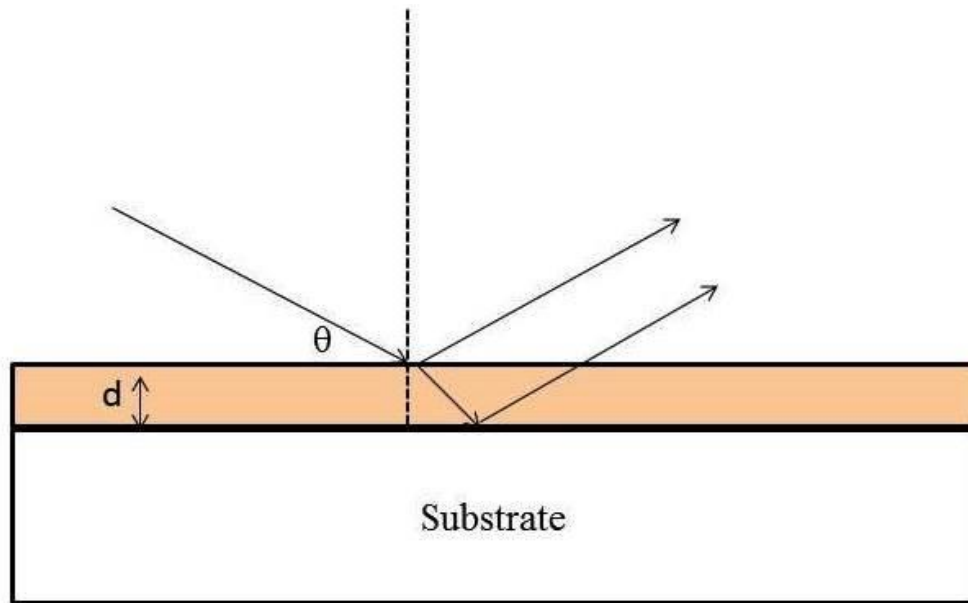
Figure 3.7: Schematic of light reflection process from a thin layer on a thick substrate [64].

Interference phenomena arise from the discontinuity of the optical medium at both the surface (air – thin film) and the interface with the substrate (thin film – substrate). The assumption of infinite substrate ensures that any reflection from the bottom boundary (substrate – air) is ignored. This simple picture assumes that the thin film is homogeneous, which is of course always the case. In a rough approximation, for an inhomogeneity smaller than the wavelength of the probing radiation, the retardation effects are neglected and the medium is still assumed homogeneous. For a film displaying well defined interference patterns as in fig 3.8 the Swanepoel method [58] is usually successful in obtaining the optical constants from the envelopes to the extrema. The top and bottom dotted lines are the envelopes on the spectrum, tangent to extrema of transmission spectrum with interference fringes. Whereas, the dotted lines in the middle is shown smooth transmission spectrum in case the luck of interference fringes due to non-uniformity in thickness.
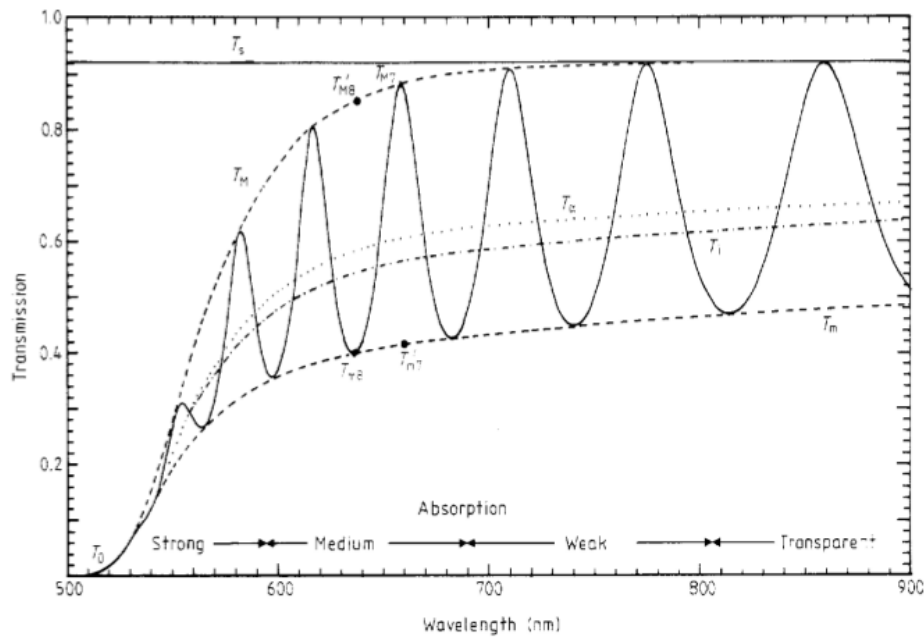
Figure 3.8: An example of a T spectrum displaying interference fringes; the top and bottom dotted lines are the envelopes on the spectrum, tangent to extrema [58].

Very thin layers can result in the lack of interference fringes and non-uniformity in thickness can result in interference fringes non-suitable for the Swanepoel method as the drawing of the envelopes results in curves that are not smoothly continuous; in such case it is necessary to fit well established electric functions to the experimental data at the same time implementing constraints specific to the film under analysis.

In Scout software [61] environment, one can input different media or materials that have specific optical constants that can be defined in the list of susceptibilities. The defined materials can be allocated to different layers stack that constitute the geometry of the layer or multilayer structures studied. The theoretical simulated spectrum (T or R) can thus be fitted to the experimental data by varying the fitting parameters i.e. the input susceptibilities.

Metals for instance, are modelled very well using the classic Drude model that describes the scattering and damping of the EM field by free charge carriers, electrons in this case. A Drude susceptibility depending on both the plasma frequency and the frequency dependent damping,

is thus implemented. In insulator oxides, UV electronic interband transitions related susceptibilities are used; if they are doped, harmonic oscillators related susceptibilities, due to absorption of impurities usually in the near-infrared are used. These oscillators describe the vibrations of atomic nuclei (much heavier than electrons) that have their resonance frequencies in the IR region.

In semiconductors, many electronic interband transitions in the UV may be required to describe them properly. In particular, for heterogeneous materials, the mixing of optical constants through the so-called effective medium concepts are often used. Maxwell Garnet [65], Bruggeman [66], Looyenga [67] and Bergman [68] are some of the examples used in Scout environment to study multi-phase composites materials.

3.6.4 The OJL-Interband Model

The OJL model proposed by O'Leary, Johnson, and Lim [69] is an empirical model, that describes the optical transitions from valence to the conduction band for amorphous semiconductor materials, upon absorption of a photon. In this mode, parabolic band edges with tail density of states that decay exponentially, are assumed as in fig 3.9.
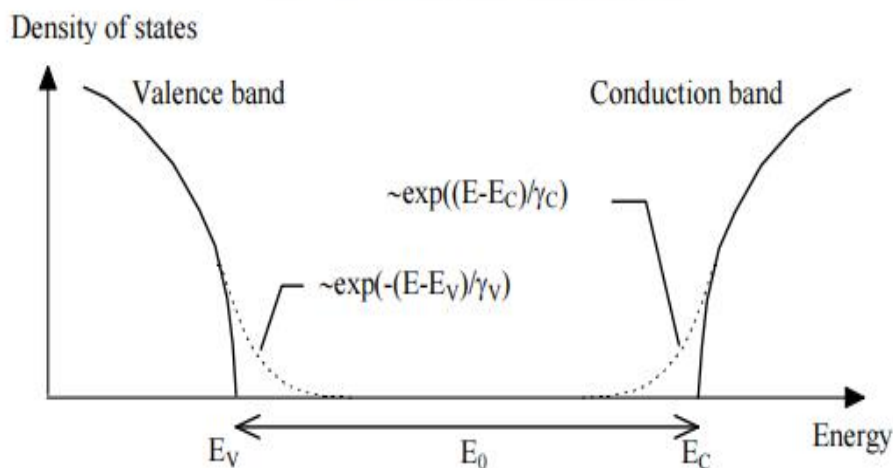

Figure 3.9: Shape of the density of states in amorphous materials near the edges of both valence and conduction bands [61].

The distribution of these tail states is related to the disorder of the network. The E_v and E_c positions at the sharp edges assume a good ordered crystalline material as shown in fig 3.10.
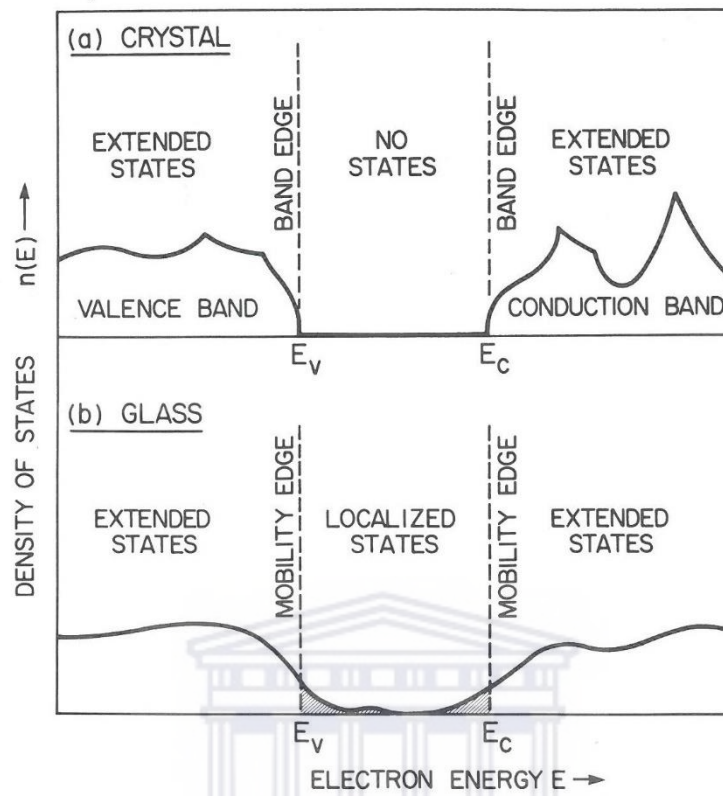
Figure 3.10: Schematic of density of states diagram for a crystalline and an amorphous semiconductor, in the vicinity of the highest occupied and lowest empty states [70].

In an amorphous semiconductor the band tailing refers to the disorder of the material that is measured by the characteristics parameters γ_c and γ_v for the conduction and valence bands, respectively. The main fitting parameters of the OJL interband transition model are the energy gap E_0, the tail state exponent of the valence band γ and the overall strength of the transition. The square of the strength fitting parameter, in Scout is proportional to the concentration of impurities in oscillators due to impurities; in this case it is proportional to the density of electrons making the transition. Fig 3.11 shows a Scout dialog window with the last three fitting parameters in cm⁻¹ units while the first one is given in $(1/cm)^{1/2}$. The decay parameter is an added scaling parameter that gives physical meaning to the imaginary part of the dielectric function that tends to increase to infinity for high values of energy.

43
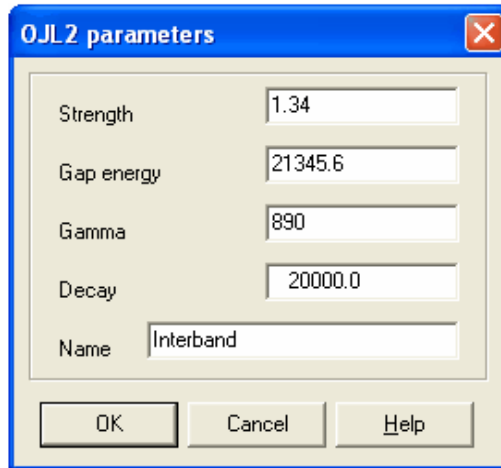
Figure 3.11: OJL fitting parameters for an amorphous semiconductor material [61].

3.6.5 Effective Dielectric Function

The optical characteristics of a heterogeneous system comprised of two or more different materials are modelled with the use of the effective medium theory. In this method, the inhomogeneities of the material can be modelled as a mixture different phases with different dielectric constants. As mentioned above however, the heterogeneous system will be considered as a homogeneous medium with a single dielectric constant if the sizes of the embedded particles are much smaller than the wavelength of the probing radiation [61]. Among those listed in the introduction of this section, the Bruggeman [66] is the most applied; often called Effective Medium Approximation (EMA). It is becoming increasingly important with an equivalent dielectric function trend to use the effect of viewing accumulated charges for varying materials of that heterogeneous composite system.

44

Volume fraction f = volume of embedded particles / total volume
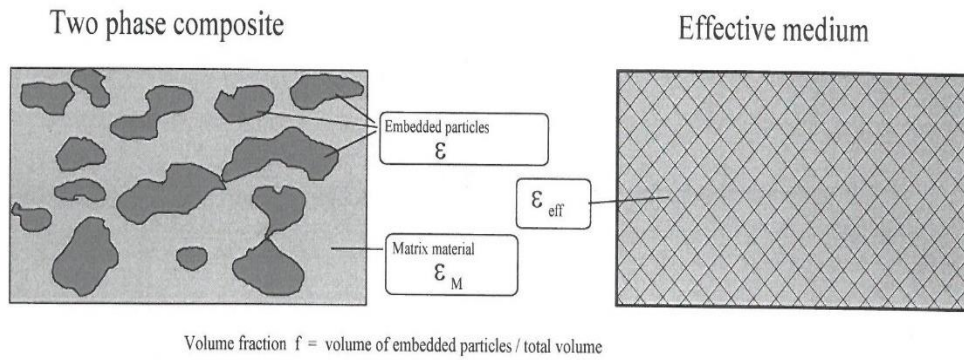
Figure 3.12: Composite system made of two different materials with two different dielectric constants (right pane); the left pane models an homogeneous material with a single effective dielectric ε_{eff} [61].

Considering a macroscopic binary composite system comprising of two materials with two different dielectric functions as shown in fig 3.12 and volume fraction f_M for the matrix and f_N for the embedded particles, it follows that:

$$f_M + f_N = 1 \qquad (3.54)$$

Assuming that the response of the two media to the electric field is not such different, we have effective dielectric function of the macroscopic system is:

$$f_M \varepsilon_M + f_N \varepsilon_N = \varepsilon_{eff} \qquad (3.55)$$

As the weightage given to the response of different dielectrics to the electric field cannot be assumed to be the same, several mixing models have been proposed as mentioned in the introductory part of this section; we will use in this study of the Bruggeman method that uses the following mixing relation [66].

45

$$(1-f)\frac{\varepsilon_m - \varepsilon_{eff}}{\varepsilon_m + 2\varepsilon_{eff}} + f\frac{\varepsilon_p - \varepsilon_{eff}}{\varepsilon_p + 2\varepsilon_{eff}} = 0 \qquad (3.56)$$

where f and ε_p are the volume fraction and the dielectric function of the embedded particles respectively.

3.6.6 Optical Energy Gap

The density of states and the conductivity of the amorphous material plays a key role in the process of the interband optical absorption. In this process, the optical excitation of electrons will be across band gap of semiconductor material. To obtain the optical band gap for the amorphous thin film a photoconductivity is consider as follows relation [71].

$$(\omega) = \frac{2\pi e^2 \; \hbar^2 \; \Omega}{m^2\omega} \int \{f(E) - f(E + \hbar\omega)\} N(E) \; |P(\omega)|^2 \; N(E + \hbar\omega) \; dE \qquad (3.57)$$

$N(E)$ and $N(E + \hbar\omega)$ are the density of states for valence and conduction bands, when the electron makes a transition from one band to another in the absorption process. Ω is the size of volume element containing one electron. $f(E)$ is Fermi-Dirac distribution and $P(\omega)$ is the constant momentum matrix element for absorption. The optical absorption strength of solid materials can be expressed as a logarithmic fraction the absorbed photons per cm^{-1}. Thus, the absorption coefficient (α) is proportional to the product of the densities of occupied and unoccupied states, which is linked by the photon energy $(\hbar\omega)$. Hence, the Fermi - Dirac distribution can be a good approximation at T = 0 for the interband transition and the photoconductivity equation simplifies as:

$$\sigma(\omega) = \frac{2\pi e^2 \; \hbar^2 \; \Omega}{m^2\omega} \int N(E) \; |P(\omega)|^2 \; N(E + \hbar\omega) \; dE \qquad (3.58)$$

The equation above may be rewritten in terms of $\alpha\ (\omega)$ as follows:

$$\alpha\ (\omega) = \frac{2\pi e^2\ \hbar^2\ \Omega}{m^2 \omega\ \varepsilon_0\ n(\omega)\ c} \int N(\mathrm{E})\ |P\ (\omega)|^2\ N(\mathrm{E} + \hbar\omega)\ d\mathrm{E} \qquad (3.59)$$

Hence, the absorption coefficient related to the conductivity is given by the following relation:

$$\alpha\ (\omega)\ = \frac{\sigma(\omega)}{\varepsilon_0\ n(\omega)\ c} \qquad (3.60)$$

As, the density of states of the valence and conduction bands are expressed by the following equations [70]:

$$N\ = N_c\ \left(\frac{\mathrm{E} - \mathrm{E}_b}{\mathrm{E}_c - \mathrm{E}_b}\right)^{\mathrm{q}},\ for\ \mathrm{E} \geq\ \mathrm{E}_b,$$

$$N = N_v\ \left(\frac{\mathrm{E}_a - \mathrm{E}}{\mathrm{E}_a - \mathrm{E}_v}\right)^{p},\ for\ \mathrm{E} \leq\ \mathrm{E}_a, \qquad (3.61)$$

Where E_a and E_b are energies of electrons in localized states in the mobility edges of the valence and conduction bands, respectively. p and q are represented the distribution of the density of states for both valence and conduction bands, respectively. If equations 3.61 and 3.60 substituting into equation 3.59 and integrating over all transitions, then the solution of the absorption coefficient can be satisfied:

$$\alpha\left(\omega\right) = \frac{2\pi e^2\ \hbar^2\ \Omega}{m^2\omega\ \varepsilon_0\ n(\omega)\ c}\cdot\frac{\Gamma(p+1)\Gamma(q+1)}{\Gamma(p+q+2)}\frac{N_v\ N_c}{(E_a-E_v)^{\ p}\ (E_a-E_b)^{q}}\langle|P(\omega)^2|\rangle\big(\hbar\omega-E_g\big)^{1+p+q} \qquad (3.62)$$

The momentum transition matrix element $P(\omega)$ for absorption is also averaged over the range of energies and assumed to be independent of ω such as:

$$[\alpha\left(\omega\right)n(\omega)\hbar\left(\omega\right)]^{1/1+p+q} =\ B_g\left(\hbar\omega-E_g\right) \qquad (3.63)$$

where B_g is a constant and E_g is the optical band gap. This relation describes Tauc band gap [72] by assuming that the density of states distribution is taken to be parabolic shape in the both valence and conduction band, where is ($p = q = \frac{1}{2}$). If the density of states distribution is taken to be linear shape, the equation above is called cubic or Bezemer gap [73], where the extrapolation $[\alpha\left(\omega\right)n(\omega)\hbar\left(\omega\right)]^{1/3}$ versus $\hbar\left(\omega\right)$ to $\alpha\left(\omega\right)^{1/3} = 0$. The plot of $[\alpha\left(\omega\right)n(\omega)\hbar\left(\omega\right)]^{1/2}$ versus $\hbar\omega$ to $\alpha\left(\omega\right) = 0$ and the extrapolation with x-axis is determined the Tauc edge for absorption level $\alpha\left(\omega\right) \geq\ 10^3$ cm^{-1}.

CHAPTER 4

Results and Discussion

This chapter presents the results of the samples studied; it is divided into two main sections: in section 4.1, we focus on the microstructural properties as obtained from FTIR, RS, XRD and SEM/EDX; the chemical bonding, crystallinity, surface morphology as well as the elemental composition properties of the films are probed. In section 2, we present the results on optical characterization; the refractive index, the absorption coefficient as well as the optical bandgap are determined.

## 4.1 Structural Properties

Films of varied thicknesses were deposited by e-beam PVD from a commercial high purity hot pressed SiC sheet of 99.99%. The deposition pressure and deposition rate were kept unchanged at $\sim 7.9 \times 10^{-6}$ mbar and 0.6 Å/s respectively, during the preparation of all the samples. The details of the samples studied are summarized in table 4.1. Thereafter, in order to induce crystallinity and improve the stoichiometry in the films, the samples were exposed to isochronal thermal annealing under vacuum at a fixed period of one hour in Ar gas atmosphere. Three temperatures of annealing were adopted: 500 ºC, 700 ºC and 1000 ºC.

Table 4.1: A summary of the deposition and annealing conditions of the samples used in this study.

Sample name	Thickness $d_{e\text{-beam}}$	Thickness $d_{X\text{-SEM}}$	Si[EDX] (at.%)	C[EDX] (at.%)	O[EDX] (at.%)	Annealing Temperature (^{o}C)
S_1	42		82.10	11.09	6.81	as-deposited
S_2						700
S_3						1000
S_4	85	207	58.62	39.32	2.05	as-deposited
S_5						500
S_6						700
S_7						1000
S_8	130	184	70.48	26.98	2.54	as-deposited
S_9						500
S_{10}						700
S_{11}						1000

4.1.1 Determination of the Thickness

For structural analysis especially when quantitative data are needed, the thickness of the layer is a required input value. In the optical spectroscopy processing, optical thickness may be simulated although an initial guess-value is required. Reliable thickness determination is thus important in thin films characterization. In e-beam PVD, the initial estimation of the thickness is given by the crystal thickness monitor; the values obtained for our samples as-deposited are presented in table 4.1. Ion beam techniques like Rutherford Backscattering Spectrometry (RBS) are used reliably to stimulate the thickness [74]; in optical techniques, the thickness is easily estimated from interference fringes if the refractive index of the material is known. The optical modelling results will be presented in section 4.2. Another reliable way of measuring directly the thickness is through microscopy techniques if the cross section is available; sharp interfaces and good integrity of the surface of the layer is needed in this case. In this thesis, cross-section SEM were done on the samples. The micrographs of S_4 and S_8 samples, as taken from different areas, are shown in fig 4.1.
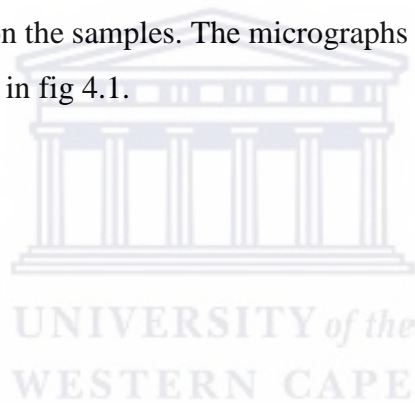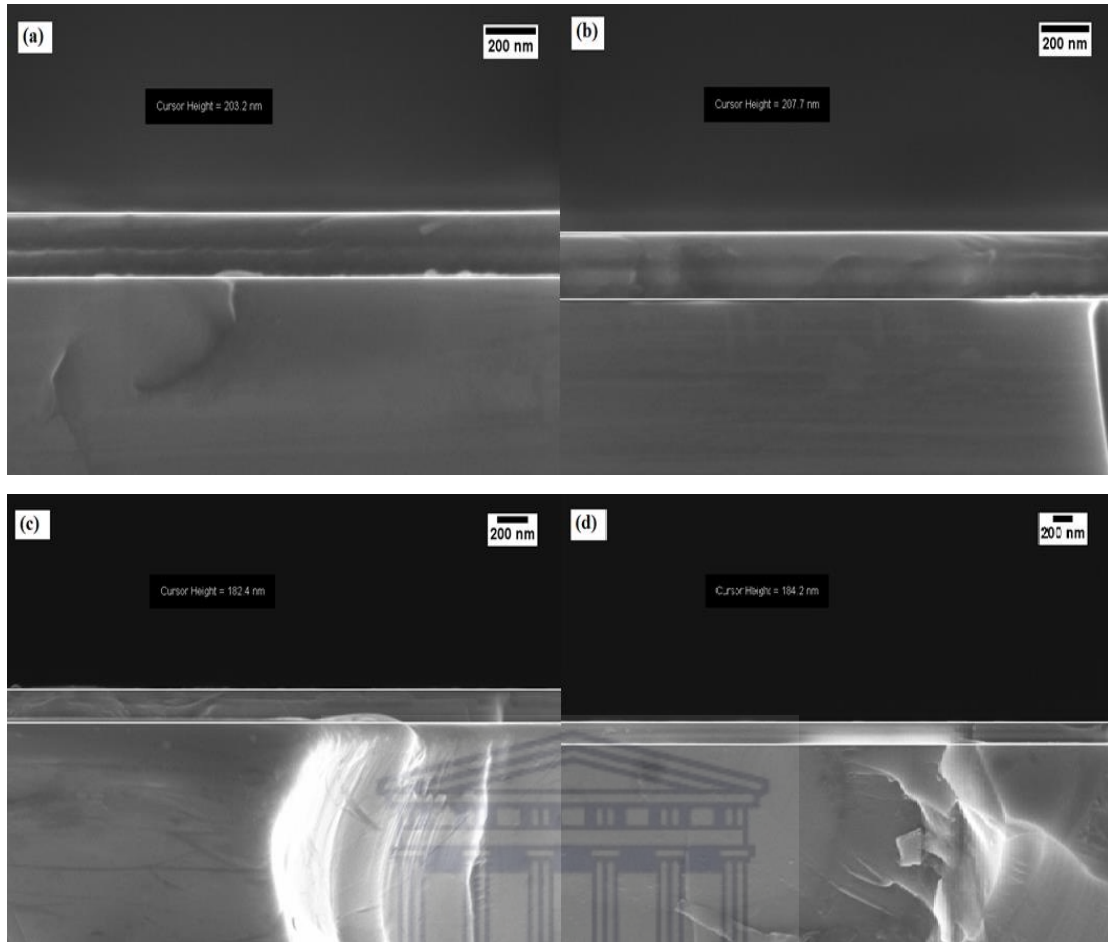
**Figure 4.1**: X-SEM images of samples S_4 (a, b) and S_8 (c, d) from two different areas.

The measured values of the thickness are indicted in table 4.1. The measured height-values are indicated on the respective images and they are listed in table 4.1. Comparing to the thickness recorded by the crystal monitor during deposition, it is clear that $d_{e\text{-beam}}$ values are systematically smaller than the $d_{X\text{-SEM}}$ ones obtained from microscopy. We can conclude that the crystal monitor tends to underestimate the thickness of the layer although errors can arise also in the measurements by X-SEM; when the layer is of the same nature as the thickness (here SiC on Si), the interface is not abrupt nor sharp and uncertainties can result. The probing beam is not normal to the specimen in X-SEM, this can be a source of overestimation. Finally, the quality of the cut specimen is of utmost importance for reliable results.

52

4.1.2 Effect of the Thickness on the Microstructure

4.1.2.1 Effect of the thickness on the microstructure by EDX analysis

Energy Dispersive X-ray Spectrometry (EDX) in SEM was utilized for analysis of chemical composition and elemental quantification in the deposited samples. Fig 4.2 shows a typical EDX spectrum of S_4 as- deposited. The main peaks present in the spectra are from Si, C, and O elements. The oxygen peak may due to surface oxidation before the deposition, residual oxygen in the deposition chamber and / or post-oxidation as the samples were analysed in the SEM days after the deposition. The carbon content was estimated to 39.32 at.%.

A summary of the elemental content of the studied films is given in table 4.1. We can conclude from the data that the films are Si rich. It has to be mentioned here that the Si content is overestimated as the substrate contributes also to the Si signal.
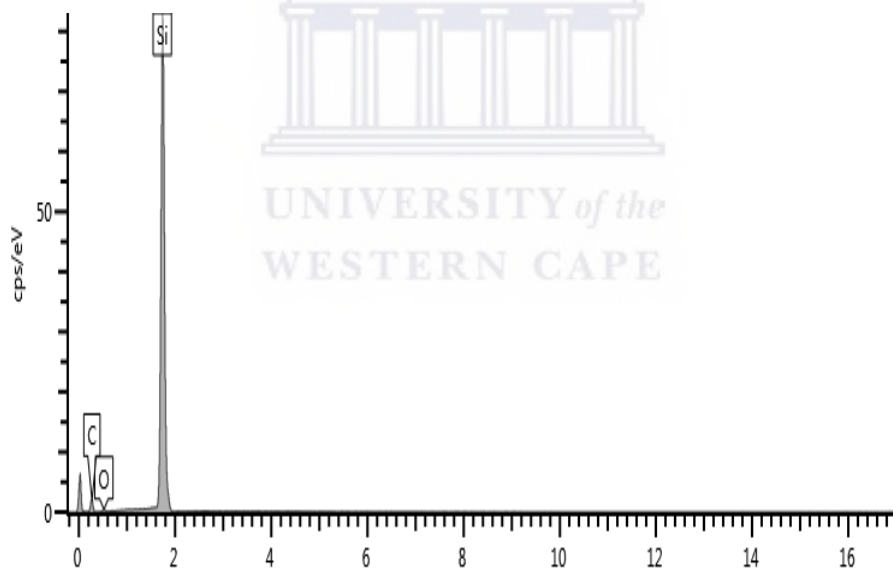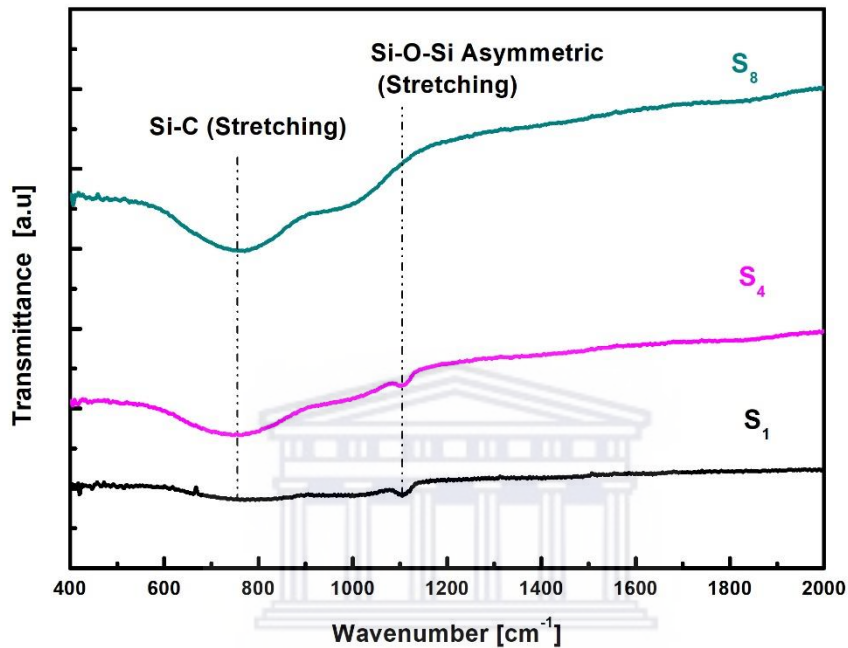

Figure 4.2: EDX spectrum of S_4 as –deposited.

4.1.2.2 Effect of the thickness on the microstructure by FTIR spectroscopy

Figure 4.3 presents FTIR transmission spectra of samples S_1, S_4 and S_8 as-deposited. The three samples are deposited on Si substrate of different thicknesses as indicated in table 4.1.

Figure 4.3: FTIR spectra of as-deposited samples S_1, S_4 and S_8.

We observe in the samples two absorption bands, one broad one centred around 754 cm^{-1} and another narrow centred 1100 cm^{-1}; the first is ascribed to Si-C stretching mode while the second is due to Si-O-Si stretching [75, 76]. The observations allow to discuss the thickness effect on the growth of SiC$_x$ films; the observations on the FTIR spectrum of S_1 suggests that the seed layer at the interface with the substrate is mainly a Si oxide layer without any sign of carbon bonding; the features observed on the spectrum of S_4 implies that the inclusion of the C atoms in the growing layer, results in the bonding mainly to Si atoms but the film remains amorphous as suggested by the broadness of the Si-C related band. The IR beam however still picks up the SiO$_x$ seed layer as suggested by the ~1100 cm^{-1} peak that remains generally unchanged. Finally, the features observed on the thickest S_8 implies the following; the sustained increase in intensity of the Si-C related band suggests that more Si and C atoms form bonds, the shift of

54

the oxidation peak to just below 1000 cm^{-1} wavenumber suggests that oxygen atoms are not only bonded to Si atoms but also to C atoms. SiC$_x$O$_{1-x}$ bonds are thus responsible to the broad band centred just below 1000 cm^{-1}. The broadness of both observed bands on the S$_8$ spectrum suggests that the film remains amorphous. We can conclude that the seed layer is dominated by oxidation, further increase in the thickness of the growing layer is dominated by C inclusion that results in Si-C bonding; the amorphous nature of the films implies the appearance of a number of dangling bonds that are passivated by oxygen atoms as the film grows thicker; this explains the shift of the 1100 cm^{-1} Si oxidation related peak to just below 1000 cm^{-1} SiC oxidation related band.

For quantification of the density of these vibrational bonds, the FTIR transmission spectrum must be converted to an absorption spectrum. The Brodsky *et al.* [50] method discussed earlier was used. The observed experimental vibrational bands have been deconvoluted into different peaks corresponding to expected theoretical vibrational modes. We have thus constrained the centres of the deconvoluted peaks to only narrow spectral regions. Accordingly, in our deconvolution process we have fixed the peaks around 740-770 cm^{-1}, 780-810 cm^{-1}, 940-1020 cm^{-1}, and 1050-1100 cm^{-1}.

Each active bond in FTIR has an associated vibration strength factor; they are found in the literature if they have been experimentally established. Those associated with Si-C at 800 cm^{-1} and Si-O at 1100 cm^{-1} have been reported to be A$_{Si-C}$ = 2.13 × 10^{19} cm^{-2} [43] and A$_{Si-O}$ = 1.5 × 10^{19} cm^{-2} [49], respectively. These strengths values combined with the integrated intensities of the respective deconvolution peaks at different wavenumbers allow to compute the bond density. The obtained data are presented in table 4.2. Whereas, other techniques such as Raman, XRD and SEM were not sensitive to the variation on the thickness of the film as-deposited.

**Table 4. 2:** Data obtained from deconvolution of FTIR spectra as- deposited of S_4 and S_8.

Sample Name	N_{Si-O} [$\times 10^{21} cm^{-3}$]	N_{Si-C} [$\times 10^{21} cm^{-3}$]	Si-C [at.%]
S_4	0.004	1.563	3.031
S_8	0.121	2.233	4.275

4.1.3 Effect of the Annealing Temperature on the Microstructure

Annealing of silicon-rich amorphous silicon carbide Si rich a-SiC$_X$ thin films has recently received great attention for application in third generation Si based photovoltaic devices [77]. The induced nanocrystals embedded in Si rich a-SiC$_X$ matrix through annealing process tune the optical bandgap of the material to higher values, making it a good candidate for window layer application in silicon multi-junction solar cells [78].

The study of SiC nanocrystals embedded in Si rich a-SiC$_X$ matrix is motivated by the successful application in devices of a variety of other materials where Si nanocrystals (SiNCs) are embedded in dielectric matrices e.g. in silicon oxide (SiO$_x$) [79] and in silicon-nitride (SiN$_x$) [80]. Compared to these dielectric matrices, the beneficial characteristic of a-SiC matrix is due to its lower bandgap of $\sim$ 2.5 eV which gives it a semiconductor character and thus better electrical transport properties [31]. However, a full understanding of the evolution of the microstructural and related changes in optical properties of amorphous Si rich a-SiC$_X$ upon thermal annealing has not yet been reached [42, 81].

4.1.3.1 Effect of the annealing temperature on the microstructure by FTIR spectroscopy
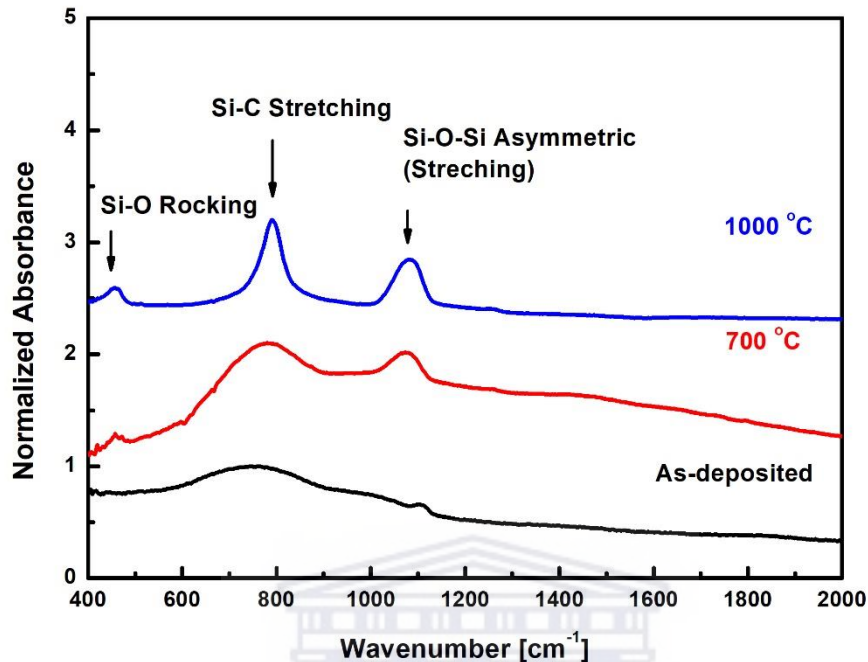

Figure 4.4: FTIR spectra of amorphous Si rich a-SiC$_X$ thin films as- deposited and annealed at 700 °C and 1000 °C for one hour.

To investigate the microstructural evolution of the films upon annealing as well as the formation of silicon and silicon carbide nanocrystals (NCs) in the amorphous silicon carbide matrix, the deposited samples have been subjected to isochronal annealing process at 700 °C and 1000 °C for one hour. FTIR spectroscopy was used to examine the evolution of the vibrational modes in the spectra of as-deposited and annealed films as well as the determination of the bond densities of (Si-C and Si-O) and carbon concentration. The experimental data were collected in transmission modes but for quantitative analysis, absorption spectra are required; the method of Brodsky, Cardona and Cuomo (BCC) [50] was adopted to convert the transmission into absorption spectra. Fig 4.4 shows the IR absorption bands of as-deposited (black curve) sample S$_4$ and as well as of those annealed at 700 °C (red curve) sample S$_6$ and 1000 °C (blue curve) sample S$_7$. We observe broad peaks in the spectral region from 600 cm^{-1} to 1100 cm^{-1}due to SiC$_x$, SiCO$_x$ and SiO$_x$ related vibration modes. They have been de-convoluted into four components cantered at 760 cm^{-1}, 800 cm^{-1}, 960 cm^{-1} and 1070 cm^{-1}

ascribed to Si-C stretching [75], Si-C stretching [43], SiCO_x (LO) [82], and Si-O stretching (TO) [76] modes, respectively.

In order to do a comparative study on the evolution of these modes with annealing, we have adopted the same boundaries around these centred - frequencies in a consistent manner for all studied samples. The de-convoluted spectra are shown in fig 4.5 [for the (a) as-deposited, (b) annealed at 700 °C and (c) annealed at 1000 °C sample].
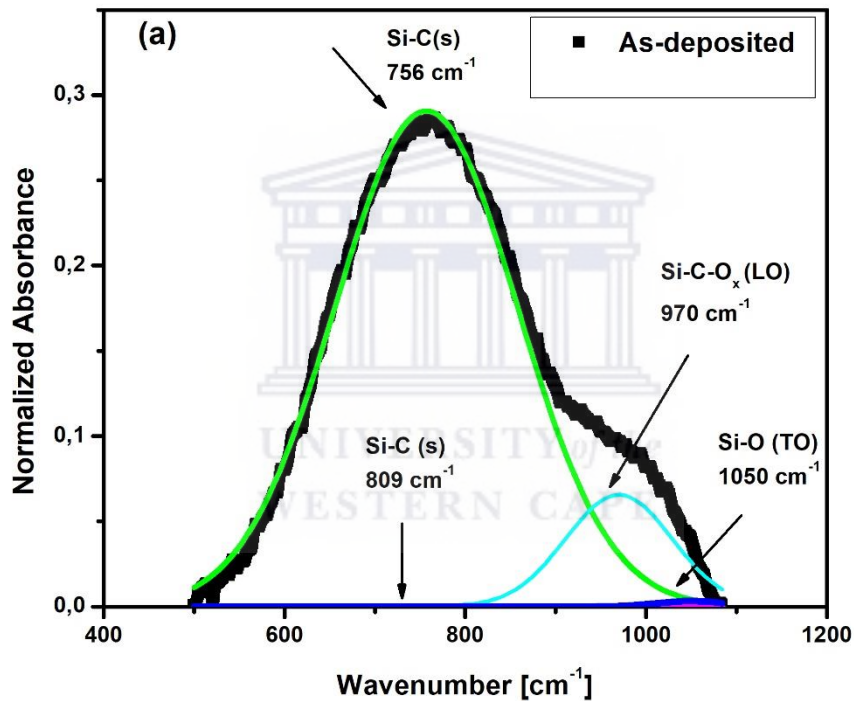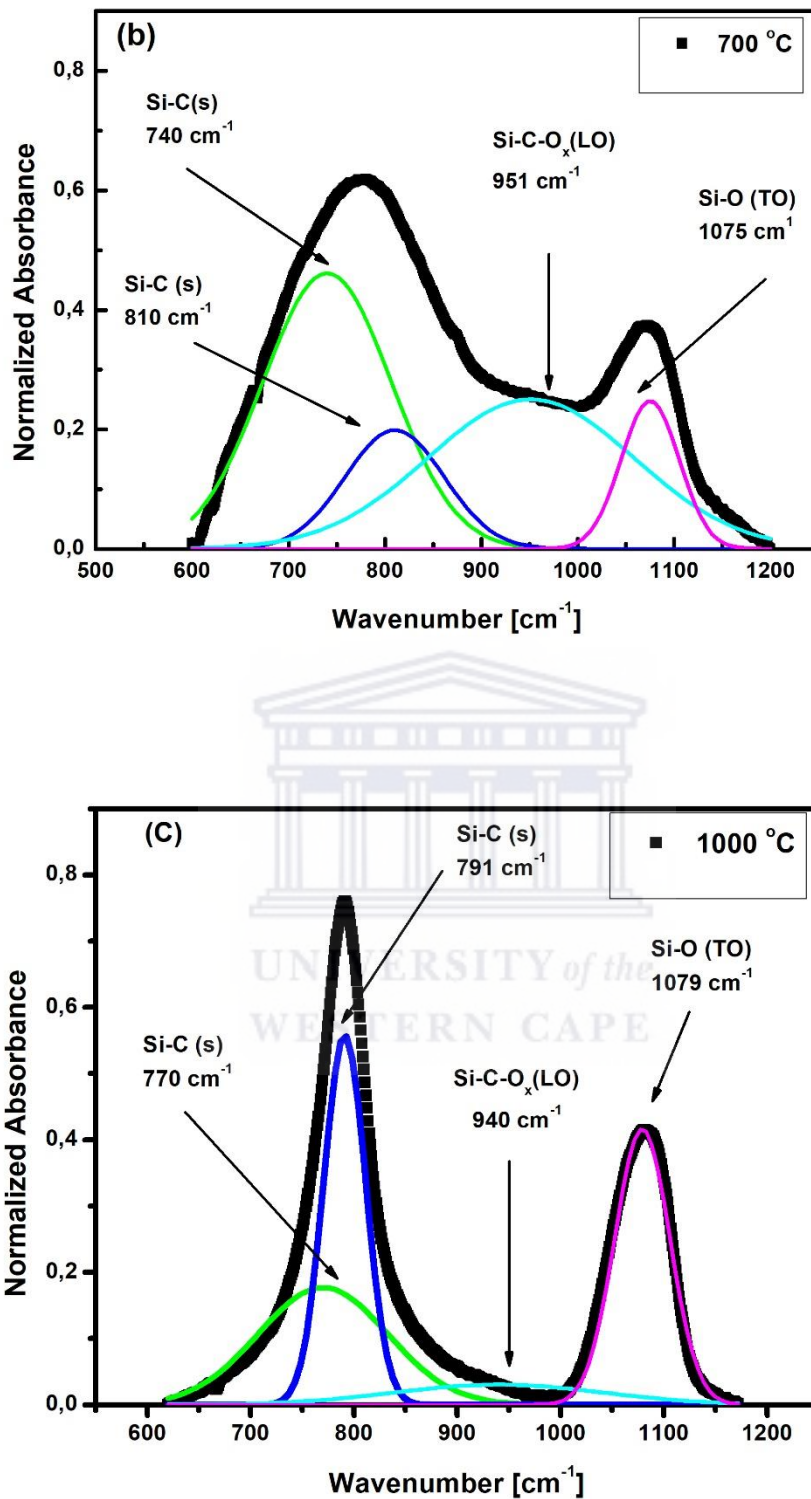
Figure 4.5: The de-convoluted FTIR spectra of sample S₄ (a) as-deposited, (b) annealed at 700 ᵒC and (c) annealed at 1000 ᵒC.

https://etd.uwc.ac.za/

The spectrum of as-deposited film has shown two major components only; SiC stretching mode centred at a low wavenumber of 756 cm^{-1} and SiC-O$_x$ centred around 970 cm^{-1}; the 800 cm^{-1} SiC was absent while the SiO stretching mode centered around 1050 cm^{-1} was negligible. On the spectrum of the sample annealed at 700 ^{o}C, in addition the above modes detected in the as-deposited sample, we noticed the emergence of a small SiC peak centred around 810 cm^{-1} and the SiO stretching mode intensified while its centre was shifting to higher wavenumbers. The spectrum of sample annealed at 1000 ^{o}C was characterized with two clearly distinct bands, narrow SiC and SiO stretching modes. The deconvolution of the SiC band revealed that the 800 cm^{-1} mode dominated over the lower wavenumber 760 cm^{-1} mode. The oxidation peak, on the other hand became more prominent and at the same time, its centre blue- shifted even further.

To quantify the bonds concentration of SiC$_x$ and Si-O$_x$ in the films, we have integrated the area under the respective components and the bond density was estimated using the following relation:

$$N_{Si-X} = A_{Si-X} \int \frac{\alpha(\omega)}{\omega} d\omega \qquad X = C, O \qquad (4.1)$$

where $\alpha(\omega)$ is the absorption coefficient for Si-X bond. A$_{Si-X}$ is the oscillating strength of the bond Si-C at 800 cm^{-1} and the Si-O bond at 1100 cm^{-1} reported to be A$_{Si-C}$ = 2.13 × 10^{19} cm^{-2} [43] and A$_{Si-O}$ = 1.5 × 10^{19} cm^{-2} [49]. The data of the calculated bond densities are summarized in table 4.3.

Table 4.3: The bond densities and carbon concertation obtained from Si-O and Si-C bonds.

Sample ID	N_{Si-O} at 1100 cm^{-1} [1x10^{21} cm^{-3}]	N_{Si-C} at 760 cm^{-1} [1x10^{21} cm^{-3}]	N_{Si-C} at 800 cm^{-1} [1x10^{21} cm^{-3}]	Si-C [at. %] atoms under 760 - 800 cm^{-1} band
S$_4$ as -deposited	0.004	1.563	0.000	3.031
S$_6$ at 700 °C	0.280	0.638	0.546	2.313
S$_7$ at 1000 ^{0}C	0.416	0.590	0.605	2.334

The data in fig 4.5 and in table 4.3 can explain the transformation and the rearrangement of the network: the gradual decrease in intensity of the SiC-O$_x$ at ~960 cm^{-1} while those of the SiC band at 800 cm^{-1} and of the SiO at 1100 cm^{-1} were increasing suggests that the reorganization of the network consisted in the breaking of the SiC-O$_x$ bonds and Si / C atoms were bonding in a much more stoichiometric manner; this is supported by the concomitant decrease in intensity of the lower energy band of the SiC stretching mode at ~ 760 °C, normally associated with disorder. This agrees with the gradual dominance of the 800 cm^{-1} SiC mode over the 760 cm^{-1} as can be seen in the evolution of their ratio in table 4.3. The narrowing of the 800 cm^{-1} band is also interpreted as a sign of better chemical order and improved crystallinity. The evolution of the band due to SiO rocking mode [83] in fig 4.4 shows that this peak is linked to crystallinity.

4.1.3.2 Effect of annealing temperature on the microstructure by Raman
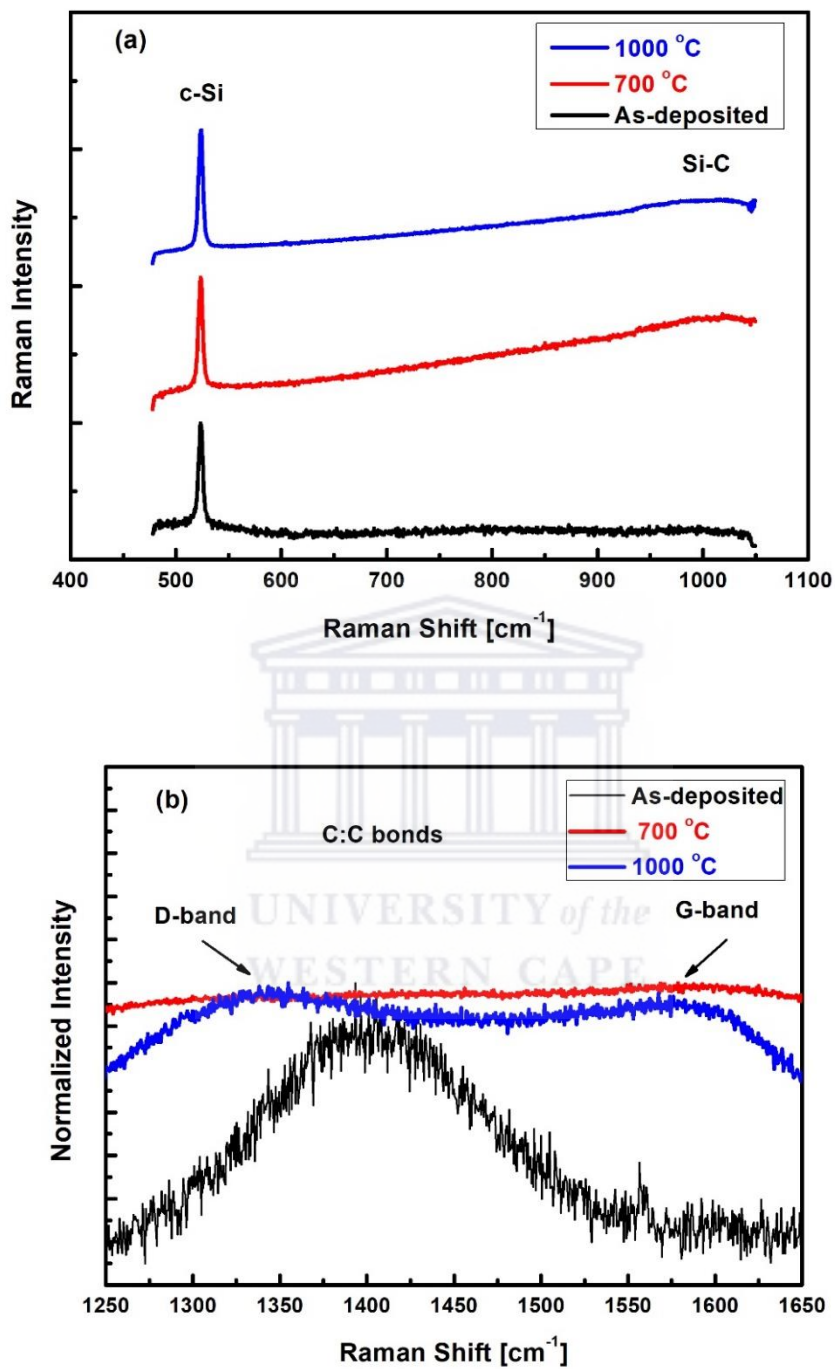
Figure 4.6: Raman spectra of amorphous Si rich a-SiC$_X$ thin films as- deposited and as-annealed at 700 ^{o}C &1000 ^{o}C for **a)** a low wavenumber **b)** a high wavenumber.

Raman spectroscopy was used as a complementary technique for structural analysis to FTIR especially in identifying the symmetric bonds, which are not active in FTIR. Fig 4.6 shows Raman spectra of amorphous Si-rich SiC thin films as deposited and annealed at (700 °C and 1000 °C) for two spectral regions, the low wavenumber from 470 cm^{-1} to 1050 cm^{-1} as seen in fig.4.6 (a) and the high wavenumber from 1250 cm^{-1} to 1650 cm^{-1} as seen in fig.4.6 (b). The low wavenumber region shows a narrow Lorentzian band centred around 523 cm^{-1} attributed to Si-Si transverse optic (TO) phonon mode in crystalline phase [84]; it is mainly due to the c-Si substrate. A weak band, whose intensity is increasing with the temperature, is observed in the region between 970 cm^{-1} and 1050 cm^{-1}; it is assigned to crystalline Si-C longitudinal optic (LO) phonon mode [85]. The higher wavenumber region shows that the Raman spectra are sensitive to the annealing temperature. In the spectrum of as-deposited sample, we observe a broad peak centred around 1400 cm^{-1}; it can be assigned to isolated disordered (D band) C-C bonds; the graphitic component (G band) around 1600 cm^{-1} is not resolved. The annealing at 700 °C makes the G band to grow in one small broad hump while the D band completely disappears; this is a sign of the improvement of order in the lattice. The spectrum of the 1000 °C annealed film was characterized of the two distinct clear bands; one centred at around 1580 cm^{-1} assigned to sp^2 bonds in the form of C-C clusters and another one with the centre wavenumber around 1340 cm^{-1} attributed to defects introduced by oxidation. Interestingly, the appearance of this D- oxidation band in the sample annealed at 1000 °C coincide with the appearance in the same sample of FTIR Si-O rocking mode mas observed just below 500 cm^{-1} in fig 4.4. This suggests that this rocking vibrating mode is due SiC$_X$O$_Y$ bonds [86].

4.1.3.3 Effect of annealing temperature on the microstructure by XRD
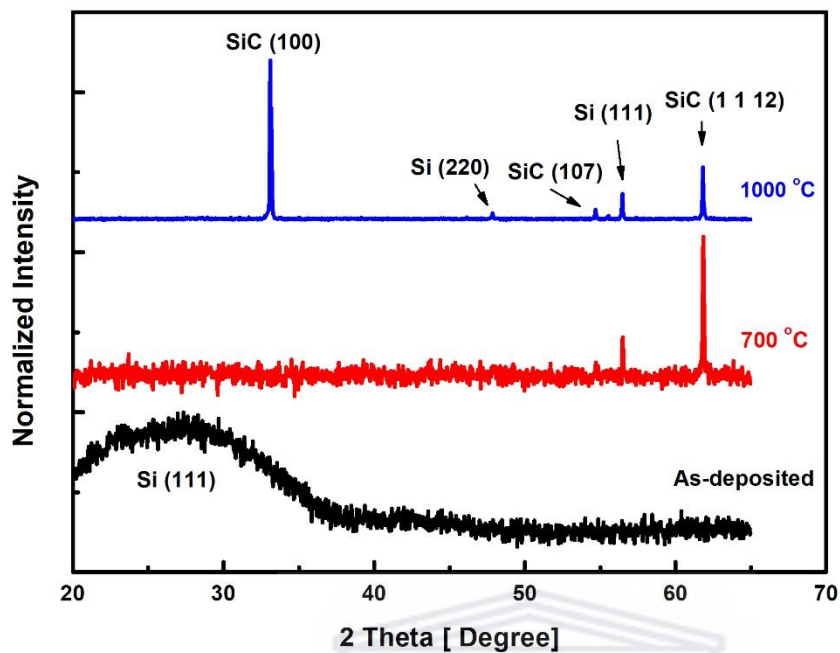
Figure 4 .7: XRD patterns of amorphous Si rich a-SiC$_X$ thin films as- deposited and annealed at 700 ºC &1000 ºC.

The crystallinity phases were investigated using XRD measurements. Fig 4.7 shows X-ray diffraction patterns of amorphous Si rich a-SiC$_X$ thin film of sample S$_4$ as deposited and sample S$_6$ and S$_7$ annealed at (700 ºC and 1000 ºC), respectively. The spectrum of as–deposited film was taken from film deposited on corning glass substrate and its displays a broad peak centered at around at 2θ = 28.5º. This peak has been assigned to Si (111) and its broadness is indicative of an amorphous structure. At the annealing temperature of 700 ºC, three diffraction peaks at 2θ = 54.7 º, 2θ = 56.4º, and 2θ = 61.8º were observed; the peaks at 54.7º and 61.8º have been matched to (107) hexagonal SiC and (1 1 12) Rhombohedral SiC, respectively. Whereas, the other peak at 2θ = 56.4º was assigned to (311) crystalline Si. In addition to the 2θ peaks at 54.7º, 56.4º and 61.8º observed in the 700 ºC annealed sample, the diffraction pattern of the sample annealed at 1000 ºC an intense peak centred at 2θ = 33.11º and a small peak at 47.8º, they have been assigned to (100) 4H-SiC and (220) Si phases, respectively. A summary of the

assignment of all the peaks observed in the annealed samples is shown in table 4.4 as processed from [87].

Table 4.4: XRD data of the identified peaks.

º2θ	khl	d-spacing (Å)	Space group	Lattice Parameter (Å)	Phase	Pattern Number	Annealing Temperature (ºC)
54.85	(107)	1.673	P63mc	a:3.0730 b:3.0730 c:15.0800	SiC	00-002-1464	700
56.48	(311)	1.629			Si	00-002-0561	700
61.83	(1112)	1.499	R3m	a:3.0730 b:3.0730 c:82.9400	SiC	00-002-1042	700
33.11	(100)	2.705	P63mc	a:3.0810 b:3.0810 c:10.0610	SiC	00-029-1127	1000
47.85	(220)	1.901			Si	00-001-0791	1000
54.68	(107)	1.678	P63mc	a:3.0817 b:3.0817 c:15.1183	SiC	01-074-1302	1000
55.51	(1040)	1.655	R3m	a:3.0730 b:3.0730 c:82.9400	SiC	00-002-1042	1000
56.45	(311)	1.63			Si	00-002-0561	1000
61.81	(1112)	1.499	R3m	a:3.0730 b:3.0730 c:82.9400	SiC	00-002-1042	1000

4.2 Optical Properties

The optical properties i.e. refractive index (n), absorption coefficient (α) and energy gap (E_g) will be determined in this section using optical models based on Scout software. The building of an optical model in Scout consists of four different steps i.e. four objects are needed: Materials, Layer stacks, Simulated Spectra and Fit parameters.

Materials, that are basically a definition of the susceptibility of the medium can be imported from the database if the optical constants are known, otherwise they are set from scratch; for a successful model, most of the time a material can be characterized by a superposition of many susceptibilities.

Layer stacks are thereafter composed as a geometrical representation of the sample optically studied; the beam is always assumed to come from a half-space made of vacuum. Materials are assigned to the individual layers.

That is these layer stacks that generate the simulated spectrum that will ultimately be fitted to the experimentally obtained spectrum by varying the fitting parameters. The quality of the fit is validated by a small value of the deviation value returned by the software. In ideal case, the deviation value should be zero but at the same time the model should be constructed in such a way that the obtained optical constants make physics sense [61].

4.2.1 The Modelling of the Substrate

For the glass substrate, two dielectric function models were needed:

- The top half-space vacuum that assumes a constant real refractive of a unity ($n = 1$) and the extinction coefficient of zero.

- The second material was a superposition of four susceptibilities: a constant refractive index in the IR of around 1.54 typical of glass, interband (IB) transition in the UV and two different oscillators. While the IB transition in the UV ensures that there is dispersion towards high energy, the other oscillators take into account of the necessary absorption, the energy gap, the disorder and some damping. Fig 4.8 shows the modelled

glass substrate where the average deviation was minimized to 0.0000771. The crystalline Si substrate was taken from the database and it was adjusted for its thickness.
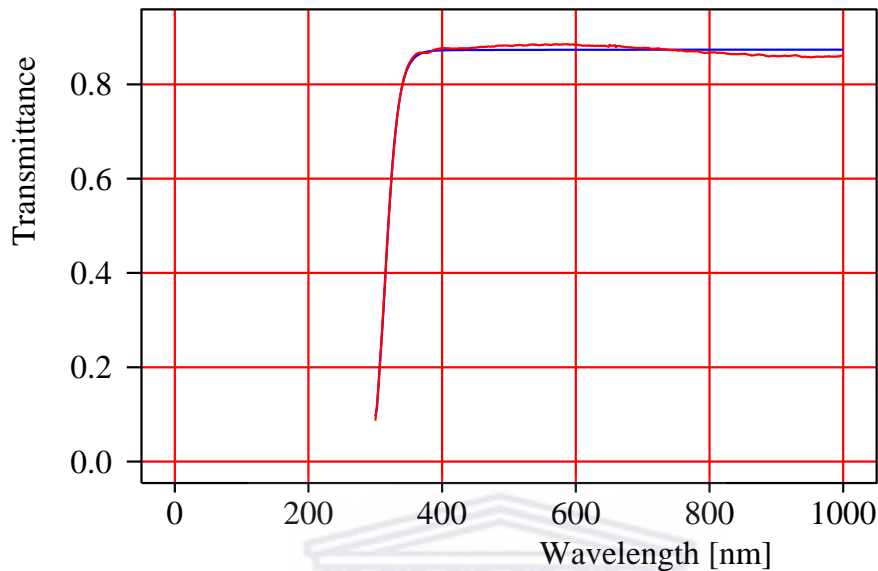

Figure 4.8: Modelling of the glass substrate used in our experiment. (The blue curve represents the simulated spectrum and the red represents the experimental spectrum).

4.2.2 Modelling of SiC interference free thin films

As mentioned in the background theory part, many researchers [58] and our group [59] have used the Swanepoel method to obtain the optical properties from films that display defined interference fringes using the interferometric relation. For films without interference though, it can be challenging to deduce the optical constant from measured transmission and reflection spectra. Fig 4.9 shows a successful modelling of a film of 146.8 nm thickness that displays no interference fringes. It has been deposited by the HWCVD process on glass substrate. In it is optical modelling, we have thus used the glass substrate as modelled in fig 4. 8 on top of the substrate, we have added in the layer stacks a thin film to which we have assigned a dielectric function built from scratch to describe a SiC film. It is "Film Material" was constructed as a superposition an interband transition function (an OJL framework that allows a mathematical model to be used to describe the density of states (DOS) of the amorphous phase), a harmonic oscillator (that allows some dispersion and at the same time caters for impurities absorption)

and a dielectric background that basically its refractive index at low energy in the infrared. A good convergence of the model allows the simulated spectrum to merge with the experimental one by minimizing the deviation value.
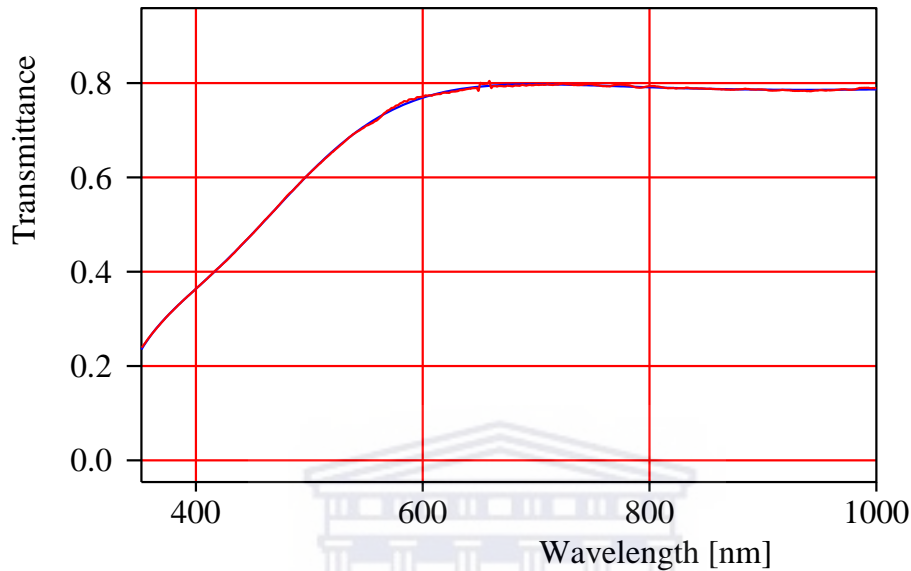

Figure 4.9: Interference free transmittance of a-SiC film 146.8 nm thick, deposited on Corning glass substrate by HWCVD; the red curve is the experimental and the blue one is the simulated. (Deviation value = 0.0000041).

One-layer stack (thin film) was considered on top of a thick substrate layer. The "Film Material" dielectric assigned to thin film was a superposition of three different dielectric functions:

- A constant refractive index in the IR
- A harmonic oscillator in the UV
- An OJL KKR dielectric

68

4.2.3 The Effect of Scattering Losses due to a Rough Interface

Fig 4.10 illustrates how the scattering losses due to interface roughness can affect the quality of the simulation if they are not corrected for. The subsequent fig 4.11 shows the improved simulation when such correction has been implemented. The procedure of it is implementation is to define a function which determines a frequency-dependent correction since the roughness scattering affects differently the radiation of different frequencies. Scattering losses are well known to be more pronounced for small wavelengths than for large ones.
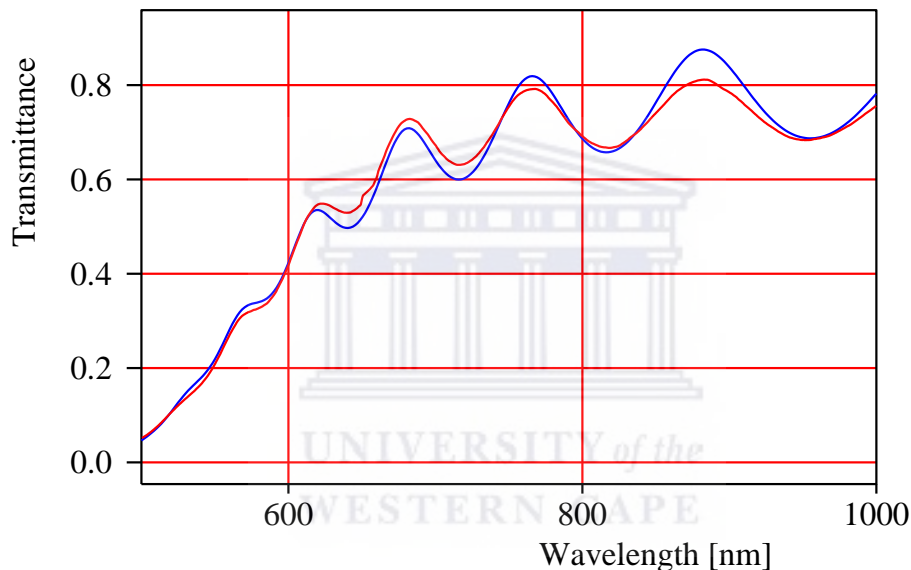
Figure 4.10: A thick SiC film of ~1250 nm modelled with the same material dielectric as in the previous example. The effect of the roughness that brings scattering losses but affecting differently the spectral range is showing. (The blue curve represents the simulated spectrum and the red represents the experimental spectrum).   (Deviation value = 0.0006231).
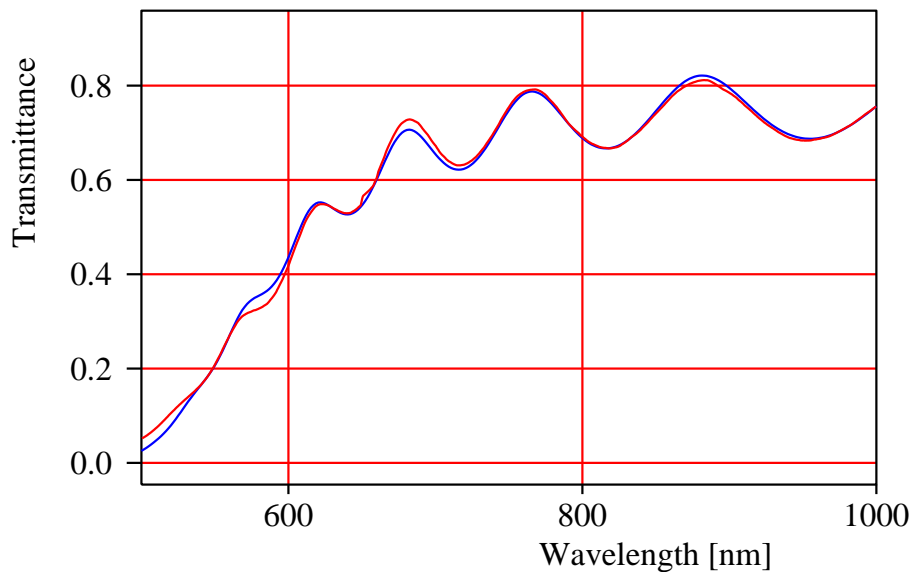
Figure 4.11: Same sample where a rough interface between the top half-space (vacuum) and the film was introduced in the layer stacks. (Deviation = 0.0001501).

4.2.4 Modelling of SiC Layers and Extraction of Optical Constants

The optical properties of SiC layers are sensitive to both the deposition conditions and the annealing process that has been used to obtain films of different stoichiometries. It is thus important to correlate the structural changes to the optical properties of the material.

A systematic modelling of e-beam PVD as deposited sample and the ones annealed have been done. Fig 4.12 displays the modelled film (S_4) as deposited. In this case, the layer stacks between two half spaces made of vacuum, a thick Si (100) substrate was assumed, as the substrate was c-Si; to account for any remaining native oxide, a thin SiOx was added at the interface with the substrate; it was followed by the main SiC layer; towards the surface, a thin porous SiC followed by a rough interface were postulated. Given the heterogeneous nature of e-beam deposited films, both the main and the porous SiC layers of the stack were assumed to be described better by an effective medium approximation (EMA) susceptibilities; as discussed above, a matrix and embedded particle media, each characterized by it is own dielectric function, coexist. As in the above example, the main SiC layer is described by a "Film Material" made of a superposition of different susceptibilities: an interband transition, a harmonic oscillator, an OJL dielectric function embedded in the so-called Kramers-Kronig

70

relation (KKR) that allow the computation of the wavelength dependent real and imaginary refractive indices from one another and finally a background constant refractive index, constant in the long wavelength and set consistently with the SiC material. The EMA functions will allow then to embed expected "particles" such as polycrystalline Si and or SiOx that can be imported directly from the database directory. To improve the flexibility and repeatability of the model to new data, we have adopted a concentration gradient to the "Film Material" assigned to the main SiC layer in the stacks. As an EMA (of Bruggeman type) was the dielectric function of this main layer, a "concentration gradient layer" assumes that the percentage of the "particle" embedded in the matrix varies along the thickness. This innovative idea made the model robust so that it can model all data of the same type. In order to make the model realist that makes physics sense, the refractive index (n_0) of the material was constrained between 2 and 3 proper to SiC materials of varied stoichiometry and the thickness below the realist value of 300 nm, expected to the very thin films grown. There is a good agreement between the simulated and experimental spectra in most part of the visible range.
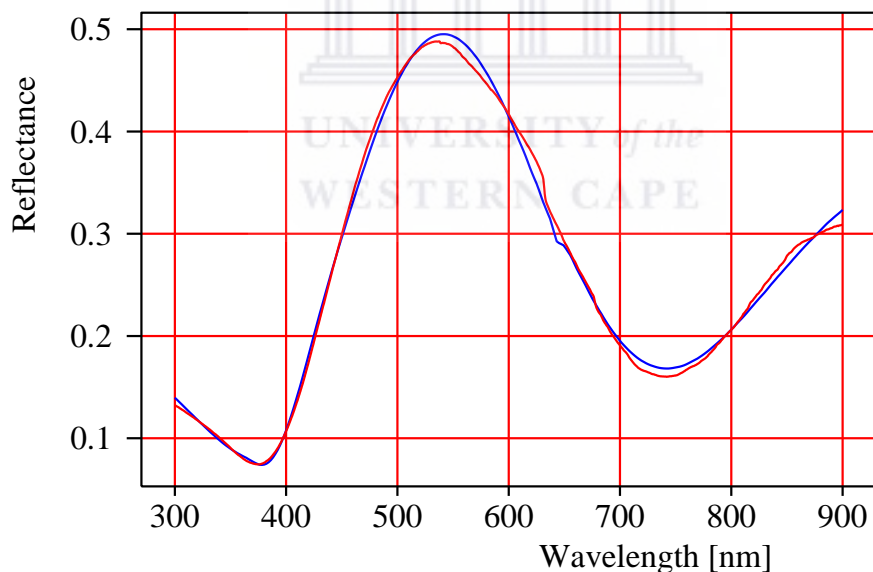
Figure 4.12: Simulated and measured reflectance spectrum of amorphous Si rich a-SiC$_X$ thin films as- deposited on c si-substrate, (The blue curve represents the simulated spectrum and the red represents the experimental spectrum). (Deviation = 0.0000545).

The thickness of the film (as read from the simulation of the main SiC layer) was estimated to be 146.3 nm. The same constructed model above was applied to the annealed films and the simulated and experimental spectra are depicted in fig 4.13.
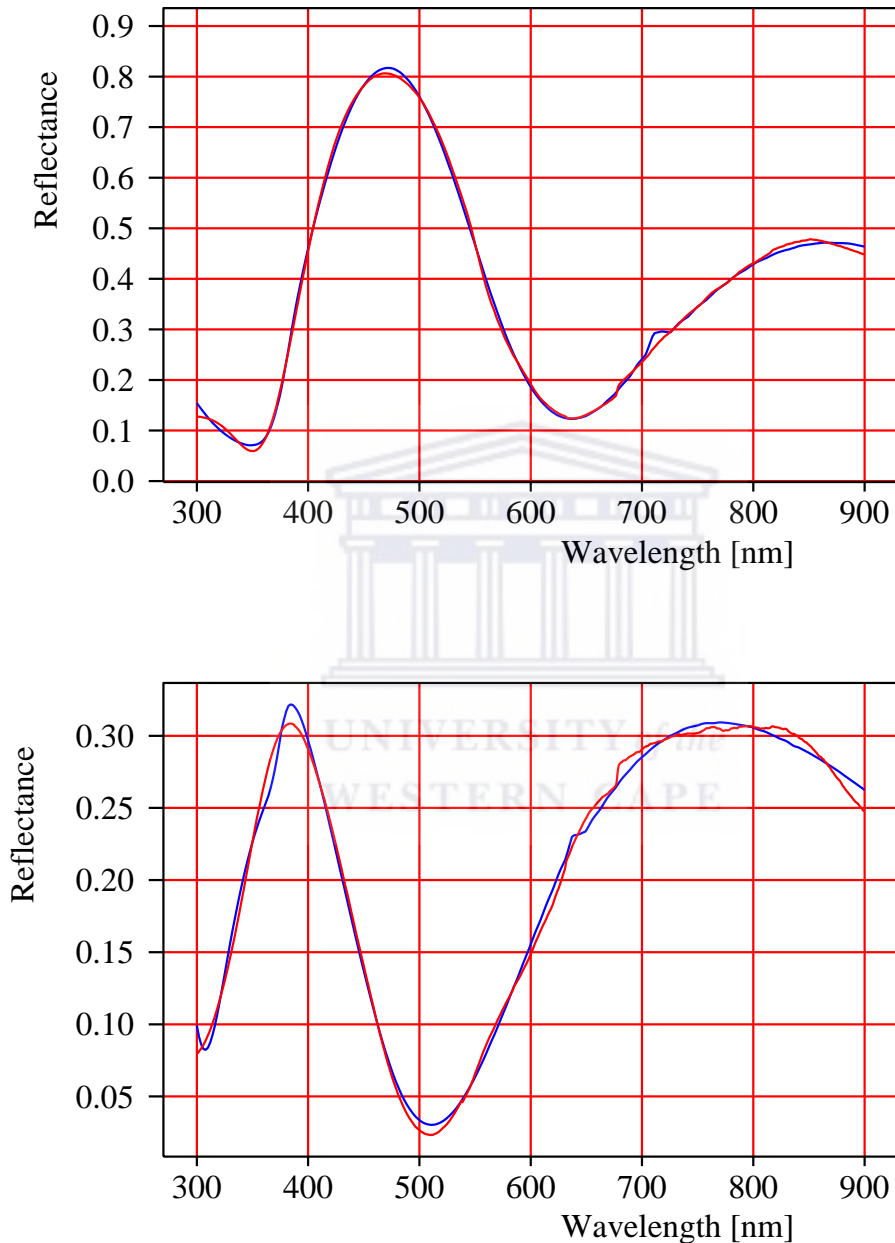
Figure 4.13: A typical modelled of an annealed films amorphous Si rich a-SiC$_X$ thin films at a) 700 ^{o}C and b) 1000 ^{o}C, (The blue curve represents the simulated spectrum and the red represents the experimental spectrum). (Deviations = 0.0000713 and 0.0000457, respectively).

All the optical parameters such as refractive index (n), absorption coefficient (α) and energy gap (E_g) have been extracted from the reflection spectra as modelled for films as deposited and as annealed at 700 °C and 1000 °C using Scout software. The obtained results are displayed in table 4.5.

Table 4.5: Optical constants extracted from Scout model for thin films as-deposited and annealed at 700 °C and 1000 °C.

| Sample (ID)	Thickness (nm)	Refractive index in the long wavelength measured at 900 nm	Absorption Coefficient at 1.3 eV (cm^{-1})	Tauc Energy Gap (eV)
S$_4$	146.4	2.3	1.0×10^4	1.8
S$_6$	126.6	2.2	4.7×10^3	2.3
S$_7$	87.4	2.1	3.2×10^3	2.5

4.2.5 Influence of the Annealing Temperature on the Refractive Index

The reported values of the refractive index of the bulk layer a-SiC$_x$ (the main SiC layer) in table 4.5 are values of the refractive index at ~1.3 eV (900 nm) i.e. in the long wavelength; conveniently we have read the values at a photon wavelength of 900 nm. Illustrative graphs of the variation of refractive index with the wavelength as well as the obtained trend with the annealing temperature are shown in fig 4.14 for sample S$_4$, S$_6$, and S$_7$. From the long to the shorter wavelength, a non-linear increasing trend is observed in all the three curves, this is the normal dispersion; a sharp decrease trend is noted towards the UV; this is the onset of absorption. This is better understood when one plots the real and imaginary parts of the

73

complex refractive index on the same figure. Fig. 4.15 displays the real (top black curve) and imaginary (bottom red curves) parts of the complex refractive index of sample S_7. On can see clearly (in the short wavelength) that the downward curvature on the real part corresponds to the upward curvature on the imaginary part. Since the imaginary part is closely related to the extinction coefficient, the rise from zero means onset of absorption. The onset of absorption blue-shifts thus with the increase of the annealing temperature. In the normal dispersion region on fig, 4.14, one can see also that the refractive curve moves to lower values as the temperature of annealing is increasing; this can be understood in terms of the density of the material; As the network crystallizes, the grain boundary regions increase in number and the network becomes porous and prone to oxidation. The amorphous tissue of as-deposited sample is thus more compact and denser and the density of the material decreases with annealing. The decrease in the density can be closely related to the porosity and increase in oxygen content; this is in agreement with our FTIR results in fig. 4.5 and table 4.3.
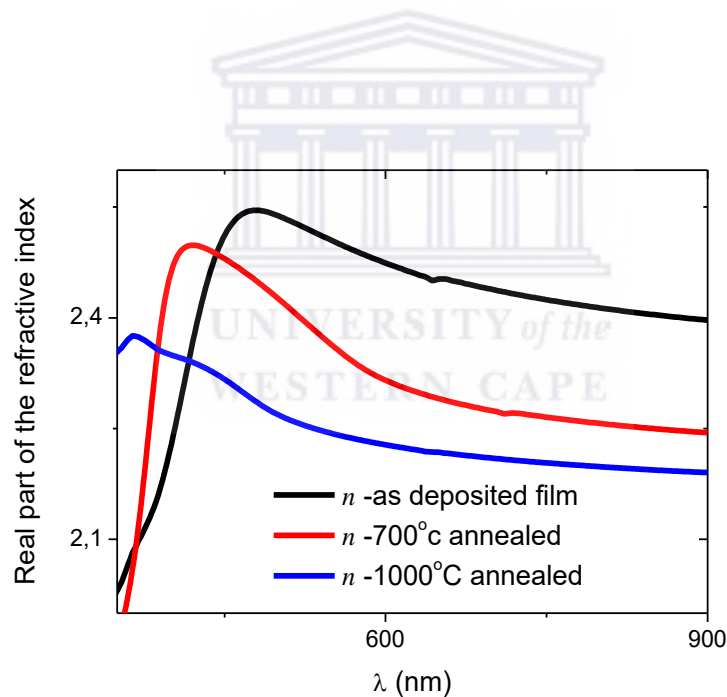

Figure 4.14: Variation of the real part refractive index (n) with annealing temperature for amorphous Si rich a-SiC$_X$ thin films.

Bruggeman DF
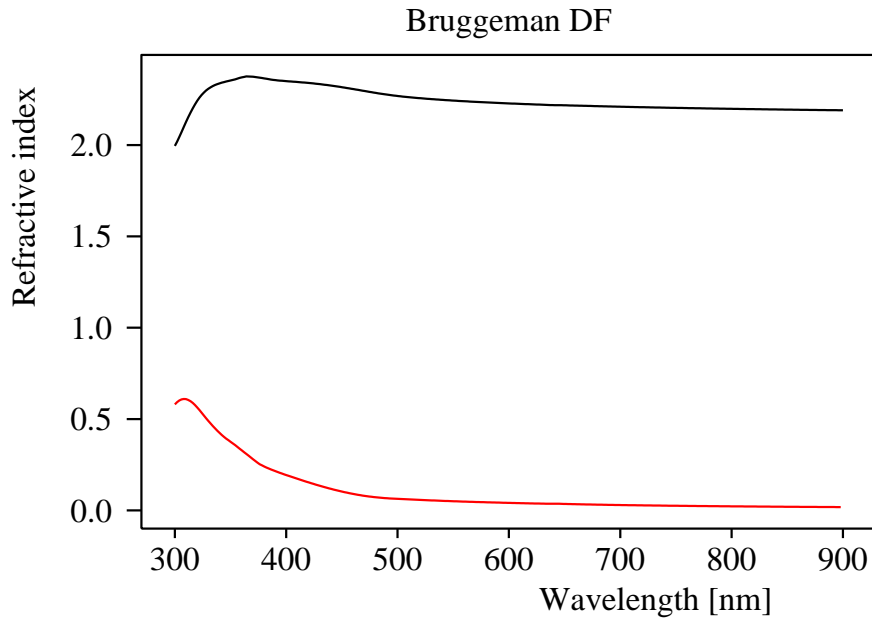
Figure. 4.15: Real and imaginary parts of the complex refractive index of sample S_7 annealed at 1000 ºC.

4.2.6 Influence of the Annealing Temperature on the Absorption Coefficient

Fig. 4.16 displays the absorption coefficient (α) curves of the samples S_4, S_6 and S_7, as-deposited and annealed at 700 ºC and 1000 ºC, respectively. The first notable fact is that the compact amorphous film as-deposited has higher values of the absorption coefficient; they decrease as the temperature of annealing is increasing; this is due to the porous structure discussed above. The second notable observation is that the onset of absorption shifts to higher photon energy as the temperature of annealing is increased. This is in agreement with the behaviour of the refractive index discussed above. We may predict from this blue-shift that the bandgap increases with the temperature of annealing and thus crystallization.

75
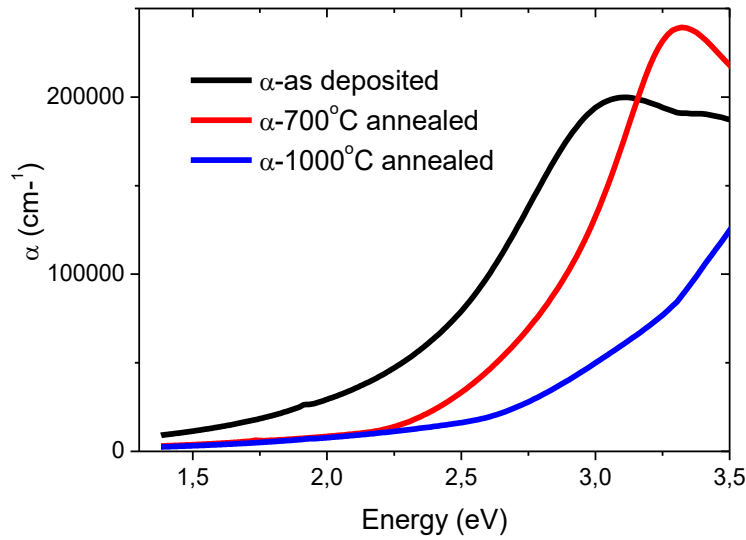
Figure 4.16: Absorption coefficient (α) versus photon energy of as-deposited sample as well as of those annealed.

4.2.7 Influence of the Annealing Temperature on the Optical Energy Gap

The empirical formula of Tauc introduced in chapter 3 has been used to determine the energy gap (E_g) by assuming a parabolic shape for the band edges. We have plotted $(\alpha h v)^{\frac{1}{2}}$ versus $h v$ and determined E_g at the cut-off with the energy axis, where $\alpha = 0$. Fig 4.17 shows the Tauc plots for samples of the thin film as- deposited and annealed at 700 ^{o}C and 1000 ^{o}C, from (a) to (c), respectively.
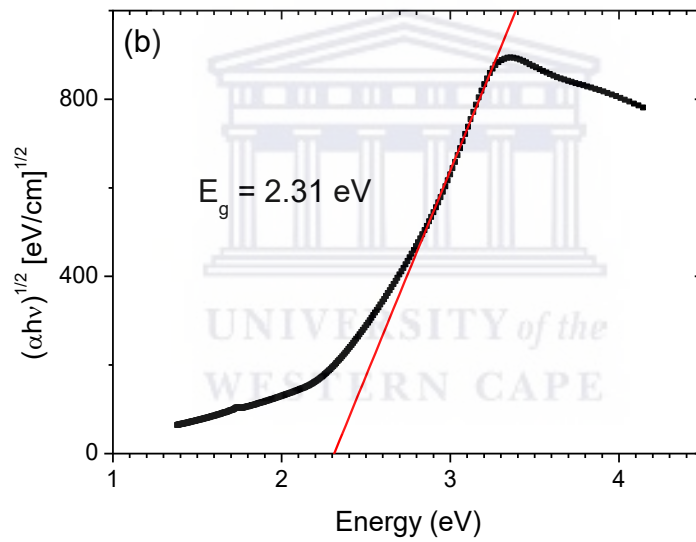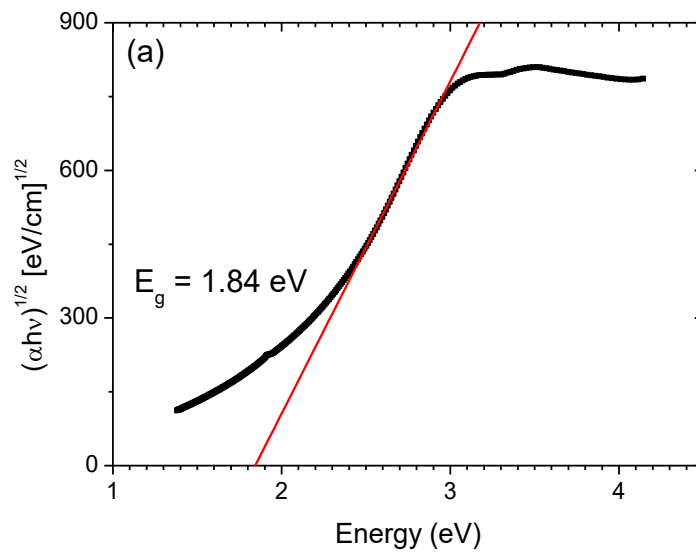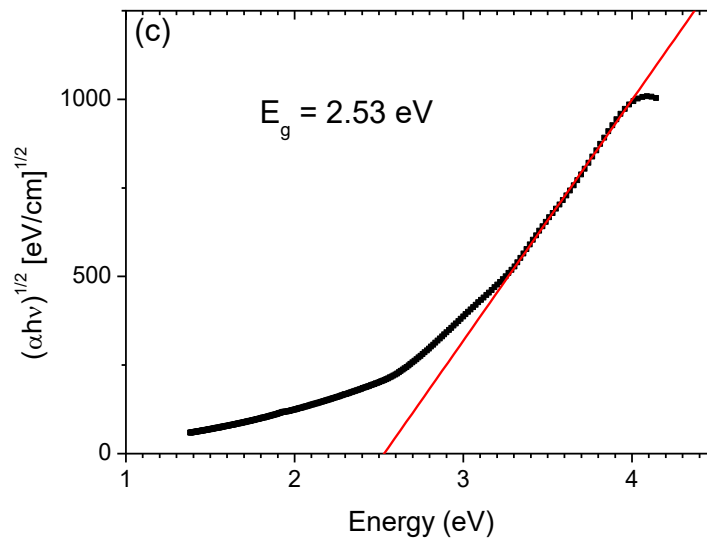
Figure 4.17: Typical Tauc plots of the studied samples: (a) as-deposited S_4, (b) annealed at 700 ^{o}C S_6 and (C) annealed at 1000 ^{o}C S_7.

E_g values of 1.84 eV; 2.31eV and 2.53 eV were extrapolated for S_4, S_6 and S_7, respectively [88, 89]. As anticipated, following the discussion above, the annealed sample at 1000 ^{o}C, with much more improved stoichiometry has higher band gap energy and thus it is transparent a larger spectral range. Fig.4.18 graphically displays the trend of E_g vs $T_{annealing}$; in other words, this is the change in E_g value (or transparency) with respect to the change in the microstructure.
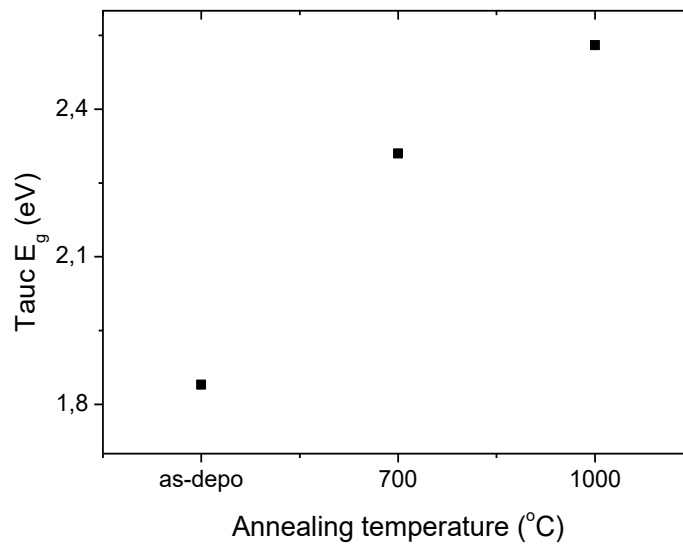
Figure 4.18 Optical band gap versus the annealing temperature

The important influence of the annealing temperature on the microstructure of the deposited thin films and the content of Si-C bonds has been discussed in the first part of this chapter. Since, the optical band gap is related to the structural change of the material, the annealing temperature will affect the values of the optical band gap as shown in fig 4.18.
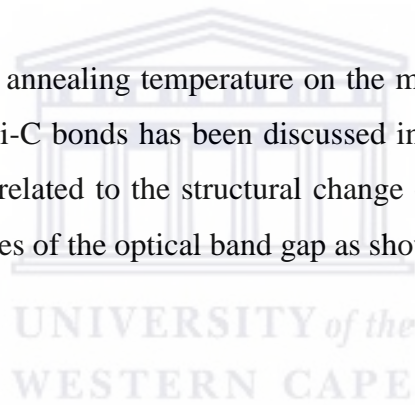
CONCLUSION AND FUTURE WORK

This thesis has studied the deposition, structural and optical characterization of non-hydrogenated amorphous silicon carbide thin film (a-SiC). Isochronal annealing process was used to induce stoichiometric changes in the films.

FTIR was found to be an instrumental technique to analyse the structural changes. A rearrangement of the microstructure through molecular vibrational spectroscopy was noted. The vibrational bands were assigned to the molecular bonds while the narrowing of the SiC related band was linked to the improved order.

Raman spectroscopy in the long wavenumber range linked the D-band to the amorphous nature of as-deposited film, while the G-band appeared with annealing. The residual D-band in the 1000 ^{o}C annealed film was linked to SiCOx rocking vibrational mode.

XRD was confirmed the amorphous structure of the as-deposited films while the appearing SiC polytypes with annealing were systematically indexed.

The last part of the thesis focused on the optical characterization of the films. We were able to build a robust optical model for SiC materials that take into account the in-homogeneities in the film through the so-called effective medium approximation (EMA) and concentration gradient by introducing a dedicated concentration gradient function in our model that was built from scratch.

In future work, the expertise acquired in modelling multi-stack layers will be very important in analysing tandem and multi-junction solar cells. Our optical model is however versatile enough to study multi-structures for other applications.

REFERENCES

[1]   C. A. Wolden, J. Kurtin, J. B. Baxter, I. Repins, S. E. Shaheen, J. T. Torvik, A. A. Rockett, V. M. Fthenakis, and E. S. Aydil, "Photovoltaic manufacturing: Present status, future prospects, and research needs," *J. Vac. Sci. Technol. A*, vol. 29, no. 3, pp. 030801, 2011.

[2]   J. D. Ouwens, "Characterization and application of wide band gap amorphous silicon," PhD Thesis, Utrecht University, Nethrlands, 1995.

[3]   "Solar Spectrum," *Solar radiation instruments information,* 2017. Available [Online]: <<:https://www.globalspec.com/learnmore/sensors-transducers-detectors/weather-sensing/solar-radiation-instruments.>>

[4]   M. A. Green, "Third generation photovoltaics : solar cells for 2020 and beyond," *Phys. E*, vol. 14, no. 1–2, pp. 65–70, 2002.

[5]   W. Shockley and H. J. Queisser, "Detailed balance limit of efficiency of p - n junction solar cells," *J. Appl. Phys.*, vol. 32, no. 3, pp. 510–519, 1961.

[6]   M. A. Green, K. Emery, Y. Hishikawa, W. Warta, and E. D. Dunlop, "Solar cell efficiency tables (version 48)," pp. 905–913, 2016.

[7]   E. Placzek-Popko, "Top PV market solar cells 2016," *Opto-Electronics Rev.*, vol. 25, no. 2, pp. 55–64, 2017.

[8]   F. Liu and R. Maboudian, "Silicon carbide micro / nano-systems for extreme environment," *Mantech Conference, May 17th-20th, 2010, Portland, Oregon, USA*.

[9]   N. Zhang, "4H-Silicon carbide PN diode for harsh environment temperature sensing applications," MSc Thesis, University of California, USA, 2014.

[10]   F. S. Tehrani, "Influence of total gas partial pressure on the structural formation of SiC thin films deposited by HWCVD technique," *J. Mater. Sci. Mater. Electron.*, vol. 27, no. 11, pp. 11457–11462, 2016.

[11] W. Ma, C. C. Lim, T. Saida, H. Okamoto, and Y. Hamakawa, "Microcrystalline silicon carbide—new useful material for improvement of solar cell performance," *Sol. energy Mater. Sol. cells*, vol. 34, no. 1–4, pp. 401–407, 1994.

[12] P. M. Sarro, "Silicon carbide as a new MEMS technology," *Sensors Actuators A*, vol. 82, no. 1–3, pp. 210–218, 2000.

[13] H. Morkoc, S. Strite, G.B. Gao, M.E. Lin, B. Sverdlov, and M. Burns, "Large - band - gap SiC, III - V nitride, and II - VI ZnSe- based semiconductor device technologies," *J. Appl. Phys.*, vol. 76, no. 3, pp. 1363–1398, 1994.

[14] S. Miyajima, A. Yamada, and M. Konagai, "Aluminum-doped hydrogenated microcrystalline cubic silicon carbide films deposited by hot wire CVD," *Thin Solid Film.*, vol. 501, no. 1–2, pp. 186–189, 2006.

[15] S. Klein, R. Carius, F. Finger, and L. Houben, "Low substrate temperature deposition of crystalline SiC using HWCVD," *Thin Solid Films.*, vol. 501, pp. 169–172, 2006.

[16] T. Chen, Y. Huang, D. Yang, R. Carius, and F. Finger, "Development of microcrystalline silicon carbide window layers by hot-wire CVD and their applications in microcrystalline silicon thin film solar cells," *Thin Solid Films*, vol. 519, no. 14, pp. 4523–4526, 2011.

[17] Z. Yu, I. Pereyra, and M. N. P. Carreno, "Wide optical band gap window layers for solar cells," *Sol. energy Mater. Sol. cells*, vol. 66, no. 1–4, pp. 155–162, 2001.

[18] F. Finger, O. Astakhov, T. Bronger, R. Carius, T. chen, A. Dasgupta, A. Gordijn, L. Houben, Y. Huang, S. Klein, and M. Luysberg, "Microcrystalline silicon carbide alloys prepared with HWCVD as highly transparent and conductive window layers for thin fi lm solar cells," *Thin Solid Films*, vol. 517, no. 12, pp. 3507–3512, 2009.

[19] S. Koo, "Design and process issues of junction- and ferroelectric- field effect transistors in silicon carbide, PhD Thesis," KTH Royal Institue of Tchnology, Sweden, 2003.

[20] R. Wu, K. Zhou, C. Yoon, J. Wei, and Y. Pan, "Progress in materials science recent progress in synthesis, properties and potential applications of SiC nanomaterials," *J. Prog. Mater. Sci.*, vol. 72, pp. 1–60, 2015.

[21] F. L. Cumbrera, A. L. Ortiz, and F. Sa, "The prolific polytypism of silicon carbide," *J. Appl. Crystallogr.*, vol. 46, no. 1, pp. 242–247, 2013.

[22] G. R. Fisher and P. Barnes, "Towards a unified view of polytypism in SiC towards a unified view of polytypism in silicon carbide," *Philos. Mag. B*, vol. 61, no. 2, pp. 217–236, 1990.

[23] G. Foti, "Silicon carbide : from amorphous to crystalline material," *Appl. Surf. Sci.*, vol. 184, no. 1–4, pp. 20–26, 2001.

[24] D. G. Mcculloch, A. R. Merchant, N. A. Marks, N. C. Cooper, P. Fitzhenry, and M. M. M. Bilek, "Wannier function analysis of tetrahedral amorphous networks," *Diam. Relat. Mater.*, vol. 12, no. 10–11, pp. 2026–2031, 2003.

[25] S. Janz, PhD Thesis, "Amorphous silicon carbide for photovoltaic applications," University of Konstanz, Germany, 2007.

[26] B. Jazizadeh, "Stoichiometric hydrogenated amorphous silicon carbide thin film synthesis using DC-saddle plasma enhanced chemical vapour deposition," MSc Thesis, University of Tronto, Canada, 2013.

[27] J. D. Reddy, "Mechanical properties of silicon carbide (SiC) thin films," MSc Thesis, University of South Florid, USA, 2008.

[28] T. Wu, H. Shen, B. Cheng, Y. Pan, B. Liu, and J. Shen, "Formation of α -Si$_{1-x}$ C$_x$: H and nc-SiC films grown by HWCVD under different process pressure," *Appl. Surf. Sci.*, vol. 258, no. 3, pp. 999–1003, 2011.

[29] F. Shariatmadr, "Hot-wire chemical vapour deposition of silicon carbide thin films from pure silanea and methane gases," PhD Thesis, University of Malaya, Malysia 2013.

[30] A. V Vasin, S. P. Kolesnik, A.A. Konchits, A.V. Rusarsky, V.S. Lysenko, A. N. Nazarov, Y. Ishikawa, and Y.Koshka, "Structure , paramagnetic defects and light-emission of carbon-rich a -SiC : H films," *J. Appl. Phys.*, vol. 103, no. 12, p. 123710, 2008.

[31] G. Conibeer, M. Green, R. Corkish, Y. Cho, E. C. Cho, C.W. Jiang, T. Fangsuwannarak, E. Pink, Y. Huang, T. Puzzer, and T. Trupke, "Silicon nanostructures for third generation photovoltaic solar cells," *Thin Solid Films*, vol. 511, pp. 654–662, 2006.

[32] M. Tabbal, A. Said, E. Hannoun, and T. Christidis, "Amorphous to crystalline phase transition in pulsed laser deposited silicon carbide," *Appl. Surf. Sci.*, vol. 253, no. 17, pp. 7050–7059, 2007.

[33] C. Ricciardi, "Microstructure analysis of a-SiC : H thin films grown by high-growth-rate PECVD," *J. Non. Cryst. Solids*, vol. 352, no. 9–20, pp. 1380–1383, 2006.

[34] A. Pawbake, A. Mayabadi, R. Waykar, and R. Kulkarni, "Growth of boron doped hydrogenated nanocrystalline cubic silicon carbide (3C-SiC) films by Hot wire-CVD," *Mater. Res. Bull.*, vol. 76, pp. 205–215, 2016.

[35] Y. Sun, T. Miyasato, J. K. Wigmore, N. Sonoda, and Y. Watari, "Characterization of 3C-SiC films grown on monocrystalline Si by reactive hydrogen plasma sputtering," *J. Appl. Phys.*, vol. 82, no. 5, pp. 2334–2341, 1997.

[36] D. Song, D. Inns, A. Straub, M. L. Terry, P. Campbell, and A. G. Aberle, "Solid phase crystallized polycrystalline thin-films on glass from evaporated silicon for photovoltaic applications," *Thin Solid Films*, vol. 513, no. 1–2, pp. 356–363, 2006.

[37] J. J. Merkel, T. Sontheimer, B. Rech, and C. Becker, "Directional growth and crystallization of silicon thin films prepared by electron-beam evaporation on oblique and textured surfaces," *J. Cryst. Growth*, vol. 367, pp. 126–130, 2013.

[38] C. Becker, T. Sontheimer, S. Steffens, S. Scherf, and B. Rech, "Polycrystalline silicon thin films by high-rate electronbeam evaporation for photovoltaic applications - Influence of substrate texture and temperature," *Energy Procedia*, vol. 10, pp. 61–65, 2011.

[39] G. V. Bunton, "Some properties of silicon carbide thin films prepared by electron beam evaporation," *J. Phys. D. Appl. Phys.*, vol. 3, no. 2, pp. 232–235, 1970.

[40]   "electron beam evaporation device.", 2019. Available [Online]: <<https://www.jeol.co.jp/en/science/eb.html.>>

[41]   C. Song, Y. Rui, .Wang, J. Xu, W. Li, K. Chen, Y. Zuo, and Q. Wang, "Structural and electronic properties of Si nanocrystals embedded in amorphous SiC matrix," *J. Alloys Compd.*, vol. 509, no. 9, pp. 3963–3966, 2011.

[42]   Z. Xia and S. Huang, "Structural and photoluminescence properties of silicon nanocrystals embedded in SiC matrix prepared by magnetron sputtering," *Solid State Commun.*, vol. 150, no. 19–20, pp. 914–918, 2010.

[43]   M. Künle, T. Kaltenbach, P. Loper, A. Hartel, S. Janz, O. Eibl, and K.G. Nickel "Si-rich a-SiC:H thin films: Structural and optical transformations during thermal annealing," *Thin Solid Films*, vol. 519, no. 1, pp. 151–157, 2010.

[44]   P. Griffiths and J. Haseth, *Fourier transform infrared spectrometry*, Second edition, John Wiley & Sons, Inc, 2007.

[45]   D. L. Pavia, G. M. Lampman, G. S. Kriz, and J. A. Vyvyan, *Introduction to spectroscopy,* Cengage Learning, 2008.

[46]   B. H. Stuart, *infrared spectroscopy fundamentals and application,* John Wiley & Sons, Inc, 2004.

[47]   J. R. Ferraro, K. Nakamoto, and C. W. Brown, *Introductory raman spectroscop,* california 92101-4495, USA: Academic Press, 525 B Street, Suite 1900, San Diego, 2003.

[48]   E. Gat, M. A. El Khakani, M. Chaker, A. Jean, S. Boily, H. Pepin, J. C. Kieffer, J. Durand, B. Cros, F. Rousseaux, and S. Gujrathi, "A study of the effect of composition on the microstructural evolution of a-Si$_x$ C$_{1-x}$: H PECVD films : IR absorption and XPS characterizations," *J. Mater. Res.*, vol. 3, no. 9, pp. 2478–2487, 1992.

[49]   P. L, S. Janz, and A. W. Bett, "Amorphous Si$_x$ C$_{1-x}$: H single layers before and after thermal annealing : Correlating optical and structural properties," *Sol. Energy Mater. Sol. Cells*, vol. 94, no. 11, pp. 1942–1946, 2010.

[50] M. H. Brodsky, M. Cardona, and J. J. Cuomo, "Infrared and raman spectra of the silicon-hydrogen bonds in amorphous silicon prepared by glow discharge and sputtering," *Phys. Rev. B*, vol. 16, no. 8, pp. 3556–3571, 1977.

[51] N. Maley, "Critical investigation of the infrared-transmission-data of hydrogenated amorphous silicon alloys," *Phys. Rev. B*, vol. 46, no. 4, pp. 2078–2085, 1992.

[52] E. Smith and G. Dent, *Modern raman spectroscopy: a practical approach,* John Wiley & Sons, Inc, 2005.

[53] M. Fox, *Optical properties of solids*, 1st edition. Oxford University Press, 2001.

[54] J. and D. G. R. William D. Callister, *Materials science and engineering*. John Wiley & Sons Pte Ltd, 2015.

[55] B. D. Cullity and S. R. Stock, *Elements of X-ray diffraction*, vol. 3. Prentice hall New Jersey, 2001.

[56] G. K. Williamson and W. H. Hall, "X-ray line broadening from filed aluminium and wolfram," *Acta Metall.*, vol. 1, no. 1, pp. 22–31, 1953.

[57] P. J. Goodhew and J. Humphreys, *Electron microscopy and analysis,* Taylor & Francis, 2001.

[58] R. Swanepoel, E. Marquez, and D. A. Minkov, "Determination of the thickness and optical constants of amorphous silicon," *J. Phys. E*, vol. 16, no. 12, p. 1214, 1983.

[59] S. Halindintwali, "A study of hydrogenated nanocrystalline silicon thin films deposited by hot-wire chemical vapour deposition (HWCVD)," PhD Thesis, Unversity of the Western Cape, South Africa, 2005.

[60] T. F. G. Muller, "Optical Modeling of Amorphous and Metal Induced Crystallized Silicon with an Effective Medium Approximation," PhD Thesis, University of the Wetern Cape, South Africa, 2009.

[61] "www.mtheiss.com." .

[62] W. A. Feibelman, "Optical reflection and transmission formulae for thin films," *J. Phys. D*, vol. 1, no. 12, p. 1667, 1968.

[63] S. G. Tomlin and E. Khawaja, "The determination of the optical constants of thin films from measurements of reflectance and transmittance at normal incidence," *J. Phys. D*, vol. 5, no. 4, p. 852, 1972.

[64] S. Jacobs, "Optical properties of annealed hydrogenated amorphous silicon nitride (a-SiNx : H) thin films for photovoltaic application," MSc Thesis, University of the Western Cape, South Africa, 2013.

[65] J. C. Maxwell-Garnett, "Colours in metal glasses and in metallic films," *Philos. Trans. R. Soc. London. Ser. A*, vol. 203, pp. 385–371, 1904.

[66] D. A. G. Bruggeman, "Dielectric constant and conductivity of mixtures of isotropic materials," *Ann. Phys.(Leipzig)*, vol. 24, pp. 636–679, 1935.

[67] H. Looyenga, "Dielectric constants of heterogeneous mixtures," *Physica*, vol. 31, no. 3, pp. 401–406, 1965.

[68] D. J. Bergman, "The dielectric constant of a composite material—a problem in classical physics," *Phys. Rep.*, vol. 43, no. 9, pp. 377–407, 1978.

[69] S. K. O'Leary, S. R. Johnson, and P. K. Lim, "The relationship between the distribution of electronic states and the optical absorption spectrum of an amorphous semiconductor: An empirical analysis," *J. Appl. Phys.*, vol. 82, no. 7, pp. 3334–3340, 1997.

[70] R. Zallen, "*The physics of amorphous aolids,* by John Wiley and Sons Inc." 1983.

[71] N. F. Mott and E. A. Davis, *Electronic processes in non-crystalline materials,* Oxford university press, 2012.

[72] J. Tauc, *in optical properties of Solid,* editor .F.Abeles, North-Holland, Amsterdam, the Netherlands, 1972.

[73] R. H. Klazes, M. Van Den Broek, J. Bezemer, and S. Radelaar, "Determination of the optical bandgap of amorphous silicon," *Philos. Mag. B*, vol. 45, no. 4, pp. 377–383, 1982.

[74]   Z. C. Feng, C. C. Tin, R. Hu, and J. Williams, "Raman and rutherford backscattering analyses of cubic Sic thin films grown on Si by vertical chemical vapor deposition," *Thin Solid Films*, vol. 266, pp. 1–7, 1995.

[75]   D. I. Tzenov, N.V., Tzolov, M.B. and Dimova-Malinovska, "Hydrogen-assisted surface reactions during the growth of sputtered a-SiC:H films," *Semicond. Sci. Technol.*, vol. 9, no. 1, p. 91, 1994.

[76]   Z. An, R. K. Y. Fu, P. Chen, and C. Lin, "Silicon carbide formation by methane plasma immersion ion implantation into silicon," *J. Vac. Sci. Technol. B*, vol. 21, pp. 1375–1379, 2003.

[77]   D. Song, E. C. Cho, Y. H. Cho, G. Conibeer, Y. Huang, S. Huang, and M.A. Green, "Evolution of Si (and SiC) nanocrystal precipitation in SiC matrix," *Thin Solid Films*, vol. 516, no. 12, pp. 3824–3830, 2008.

[78]   S. Y. Myong, S. S. Kim, and K. S. Lim, "In situ ultraviolet treatment in an Ar ambient upon p-type hydrogenated amorphous silicon-carbide windows of hydrogenated amorphous silicon based solar cells," *Appl. Phys. Lett.*, vol. 84, no. 26, pp. 5416–5418, 2004.

[79]   M. Zacharias, J. Heitmann, R. Scholz, U. Kahler, M. Schmidt, and J. Bläsing, "Size-controlled highly luminescent silicon nanocrystals: A SiO/SiO_2 superlattice approach," *Appl. Phys. Lett.*, vol. 80, no. 4, pp. 661–663, 2002.

[80]   T. W. Kim, C. H. Cho, B. H. Kim, and S. J. Park, "Quantum confinement effect in crystalline silicon quantum dots in silicon nitride grown using SiH_4 and NH_3," *Appl. Phys. Lett.*, vol. 88, no. 12, pp. 23–25, 2006.

[81]   G. Wen, X. Zeng, W. Liao, and C. Cao, "Crystallization mechanism of silicon quantum dots upon thermal annealing of hydrogenated amorphous Si-rich silicon carbide films," *Thin Solid Films*, vol. 552, pp. 18–23, 2014.

[82]   O. Pluchery and J. Costantini, "Infrared spectroscopy characterization of 3C – SiC epitaxial layers on silicon," *J. Phys. D*, vol. 45, p. 495101, 2012.

[83]   Z. An, R. K. Y. Fu, P. Chen, W. Liu, P. K. Chu, and C. Lin, "Fabrication of silicon carbide thin films by plasma immersion ion implantation with self-ignited glow discharge," *Thin Solid Films*, vol. 447–448, no. 03, pp. 153–157, 2004.

[84]   Y. H. Wang, J. Lin, and C. H. A. Huan, "Multiphase structure of hydrogenated amorphous silicon carbide thin films," *Mater. Sci. Eng. B Solid-State Mater. Adv. Technol.*, vol. 95, no. 1, pp. 43–50, 2002.

[85]   H. Shen, T. Wu, Y. Pan, L. Zhang, B. Cheng, and Z. Yue, "Structural and optical properties of nc-3C-SiC films synthesized by hot wire chemical vapor deposition from SiH 4-C 2H 2-H 2 mixture," *Thin Solid Films*, vol. 522, pp. 36–39, 2012.

[86]   V. Nikas, N. Tabassum, and B. Ford, "Strong visible light emission from silicon-oxycarbide nanowire arrays prepared by electron beam lithography and reactive ion etching," *J. Mater. Res.*, no. 23, pp. 3692–3699, 2015.

[87]   A. B. V. Almelo, "X'Pert HighScore,." The Netherlands, p. Version 2.2c (2.2.3), 2007.

[88]   A. Keffous, K. Bourenane, M. Kechouane, N. Gabouze, and T. Kerdja, "Morphological, structural and optical properties of thin SiC layer growth onto silicon by pulsed laser deposition," *J. Vac.*, vol. 81, pp. 632–635, 2007.

[89]   Q. Cheng, S. Xu, and K. Ken, "Single-step , rapid low-temperature synthesis of Si quantum dots embedded in an amorphous SiC matrix in high-density reactive plasmas," *Acta Mater.*, vol. 58, no. 2, pp. 560–569, 2010.